Chair of Materials Physics

Master's Thesis

The anneal hardening phenomenon in the nanostructured Ti-Nb-Zr system

Emile Verhoestraete

August 2024

MONTANUNIVERSITÄT LEOBEN
www.unileoben.ac.at

AFFIDAVIT

I declare on oath that I wrote this thesis independently, did not use any sources and aids other than those specified, have fully and truthfully reported the use of generative methods and models of artificial intelligence, and did not otherwise use any other unauthorized aids.

I declare that I have read, understood and complied with the "Good Scientific Practice" of the Montanuniversität Leoben.

Furthermore, I declare that the electronic and printed versions of the submitted thesis are identical in form and content.

Date 09.08.2024

Signature Author
Emile Verhoestraete

Preface

This thesis concludes my 5-year journey of becoming a Material Scientist / Engineer. I feel incredibly grateful for my family, friends, roommates and my boyfriend, who have always supported me along the way.

Also, I am thankful that I was able to spend the past year in Leoben, where I have gotten into touch with many incredible people and made unforgettable memories.

I want to thank Markus and Stefan for their useful advice and for helping me perform the experiments presented here, as well performing EDX and TEM.

Writing this thesis, my insight into materials has vastly increased and I hope to continue learning and discovering in future years!

Emile Verhoestraete

Contents

Abstract

β-Ti alloys are finding their way into applications across various engineering fields, such as aerospace and the biomedical field. These alloys stand out because of their excellent mechanical properties, corrosion resistance, and their potential to match the low elastic modulus of bone tissue, which is important for implants. However, these critical applications also require high strength, to prevent failure. Hence, this thesis explores strengthening by annealing in high-pressure torsion (HPT) processed β-Ti-Nb-Zr alloys. Both severe plastic deformation processes like HPT and subsequent annealing are believed to have a positive effect on the material strength. While the hardening effects resulting from the grain size refinement induced by HPT is well-studied in β-Ti alloys and generally well-understood, the anneal hardening phenomenon and its underlying mechanisms remain a topic of discussion in literature. For this, this thesis presents the first analysis of the anneal hardening kinetics in this ternary alloy system, aiming to contribute to a better understanding of the anneal hardening phenomenon.

List of Figures and Tables

List of Figures

List of Tables

List of Abbreviations and Symbols

Abbreviations

BCC	Body-Centered Cubic
CP	Commercially Pure
DSC	Differential Scanning Calorimetry
EDX	Energy-Dispersive X-Ray Spectroscopy
FWHM	Full Width at Half Maximum
GBM	Grain Boundary Migration
HPT	High-Pressure Torsion
Mo-Eq.	Molybdenum-Equivalent
NC	Nanocrystalline
RD	Rolling Direction
SPD	Severe Plastic Deformation
TEM	Transmission Electron Microscopy
UFG	Ultra-Fine Grained
XRD	X-Ray Diffraction

Symbols

ΔH	Hardness Change: annealed - as-HPT
d	Diameter
g	Gravitational Constant
k	Anneal Hardening Rate
k_B	Boltzmann Constant
n	Number of Hardness Indents or Number of HPT Rotations
r	Radial Distance
s	Sample Standard Deviation
t	Thickness (sample dimensions) or Annealing Time
A	Pre-Exponential Constant in Arrhenius Equation
H	Hardness
Q	Activation Energy
R	Ideal Gas Constant
T	Temperature

Chapter 1

Introduction

1.1 β-Ti-alloys : Applications

The term β-Ti-alloys denotes titanium alloys that retain beta phase (body-centered cubic, BCC) upon water-quenching from the β-single phase field to room temperature [36]. These alloys contain β-stabilizing elements such as molybdenum and niobium.

β-Ti-alloys possess useful properties, including high strength-to-weight-ratio and corrosion resistance. These properties benefit both aerospace and biomedical applications [43, 9]. The following paragraphs detail the benefits of Ti-alloys, and further improvements that can enhance their application potential in these fields.

1.1.1 Biomedical applications

Biomedical materials need to fulfill a vast set of requirements, not only including mechanical properties and tissue compatibility, but also ease of manufacturing and cost [28, 43]. Multiple decades of material development have considered β-Ti-alloys as implant material, due to its excellent performance in multiple criteria. The following highlights some key requirements.

β-Ti-alloys generally have lower elastic modulus than α + β-Ti-alloys like Ti-6Al-4V, and other implant materials such as stainless steels and Co-Cr-Mo alloys [43, 41]. Low elastic modulus enhances bio-compatibility by reducing the elastic mismatch between bone and implant. A large mismatch leads to inhomogeneous stress transfer, known as stress-shielding, which may result into loosening of the implant or bone refracturing [51, 43]. Overall, similar bone and implant stiffness should increase comfort of the patient and extend the device lifetime.

Biocompatibility and corrosion resistance are two significant and interrelated material requirements [43]. Generally, titanium alloys form protective oxide layers, resulting in low corrosion rates. Still, ions released during corrosion can cause allergic reactions, or may be poisonous to the human body. The alloying elements considered in this thesis -Ti, Nb and Zr- are non-cytotoxic, in contrast to Al and V, used in the popular Ti-6Al-4V alloy. Furthermore, Kovacs and Davidson found that Ti-13Nb-13Zr (wt.%) releases less ions than Ti-6Al-4V during corrosion [38].

Current research on β-Ti-alloys for biomedical applications focuses on developing alloys with even lower elastic modulus, to further bridge the gap between implant and bone stiffness. Additionally, thermomechanical treatments that increase strength while maintaining low modulus are another area of interest [41].

1.1.2 Aerospace applications

The properties of β-Ti-alloys mentioned above are also valuable for certain applications in aerospace industry. For example, the combination of low density, high strength, low modulus, good fatigue performance and high corrosion resistance is ideal for springs and high-strength fasteners [9, 20, 77]. Additionally, β-Ti-alloys have excellent work-hardenability, and are better suited for sheet-based manufacturing than α and α + β-Ti-alloys [62]. Consequently, parts can be easily formed (e.g. by forging) in single-phase β-state, and subsequent aging heat treatments can provide additional strengthening. Continuous development of titanium alloys and research on their thermomechanical processing has resulted in increased usage of these alloys in aircraft since the 1960's [77].

In summary, β-Ti-alloys, offer significant advantages in fields such as biomedical and aerospace engineering. Of course, both applications require high material strength, to avoid failure. This thesis will thus explore a route to strengthen the material that does not rely on a second phase, which is critical to maintain low modulus [72].

1.2 Thesis Aim

This thesis aims to quantify the strengthening potential of high-pressure torsion (HPT) with subsequent annealing, using a wide range of annealing temperature and annealing duration. Specifically, three β-Ti alloys in the Ti-Nb-Zr ternary alloy system are explored here. We expect that both HPT and annealing will contribute to enhance strength of these alloys.

Chapter 2

Literature Review

This literature review aims to outline the research context of this thesis. It provides a brief overview on (meta)stable β-Ti-alloys, which are subject of this thesis' research. The review considers the relevant thermodynamics first. Next, the concept of severe plastic deformation (SPD) is introduced, focusing on high-pressure torsion (HPT), the main mechanical processing method of this thesis. The final section reviews the anneal hardening phenomenon in ultrafine grained and nanostructured metals and alloys.

2.1 β-Ti-alloys: Thermodynamics

The thermodynamics of β-Ti-alloys are briefly evaluated, to help interpret experimental results. As mentioned previously, β-Ti-alloys are titanium alloys that contain a sufficient amount of β-phase stabilizing-elements, such as molybdenum or niobium, to retain at least some or all β-phase upon quenching from high-temperature, single-phase β to room temperature. The following paragraphs introduce both equilibrium and non-equilibrium phases in β-stabilized Ti-alloys. The paragraphs thereafter touch on the molybdenum-equivalence concept and apply it on the ternary alloy system used in this thesis.

β-Ti-alloys can be classified based on the stability of the beta phase [36]. The T_β transus temperature distinguishes metastable β-alloys from stable β-alloys, it defines the temperature that separates the α + β-equilibrium phase field from single phase β. The transus temperature of stable β-Ti-alloys lies below room temperature, as indicated on the phase diagram in Figure 2.1. Other alloys are known as metastable β-alloys, these alloys form 100 % β-phase fraction when quenched from above transus temperature to room temperature, even though α + β is the equilibrium microstucture [36].

Figure 2.1 is an example of a generalized phase diagram for (isomorphous) binary β-Ti-alloys [36]. Some β-stabilized binary Ti-alloys display similar behavior, but eutectoid binary systems exist as well, such as Ti-Cr and Ti-Fe. Such cases will not be discussed here, because Ti-Nb is not an eutectoid system [26]. The Ti-Zr

system, Figure 2.2, in contrast, has a single phase-HCP region in equilibrium at room temperature, up to at least 600 °C [26].

2.1.1 Non-equilibrium phases

Slow decomposition kinetics of β-phase below the transus temperature results in formation of non-equilibrium phases, such as α', α" and ω [47]. The green phase diagram in Figure 2.3 includes these non-equilibrium phases in the binary Ti-Nb system [8]. All can be formed upon water-quenching from above β-transus temperature to room temperature, by a displacive transformation [47, 4]. Phases that result from displacive transformations are reffered to as *athermal*.

Additionally, the above phases also have diffusive variants, meaning they can be precipitated during heat treatments [6, 7, 52]. In that case, they are referred to as *isothermal*. Thus, it is possible that these phases form during the aging treatments in this work. Moreover, the ω-phase can be induced by high pressure as well, which has been observed in both commercially pure titanium and Ti-Nb alloys [53, 78].

2.1.2 Molybdenum-equivalent expressions

The similarity among phase diagrams of β-stabilized Ti-alloys allows to compare the stabilizing effect of different alloying elements. The molybdenum-equivalent (Mo-eq.) expresses this effect relative to the effect of molybdenum in Ti-Mo alloys [36, 45]. Most equations attribute a certain coefficient, i.e. a weight, to each alloying element,

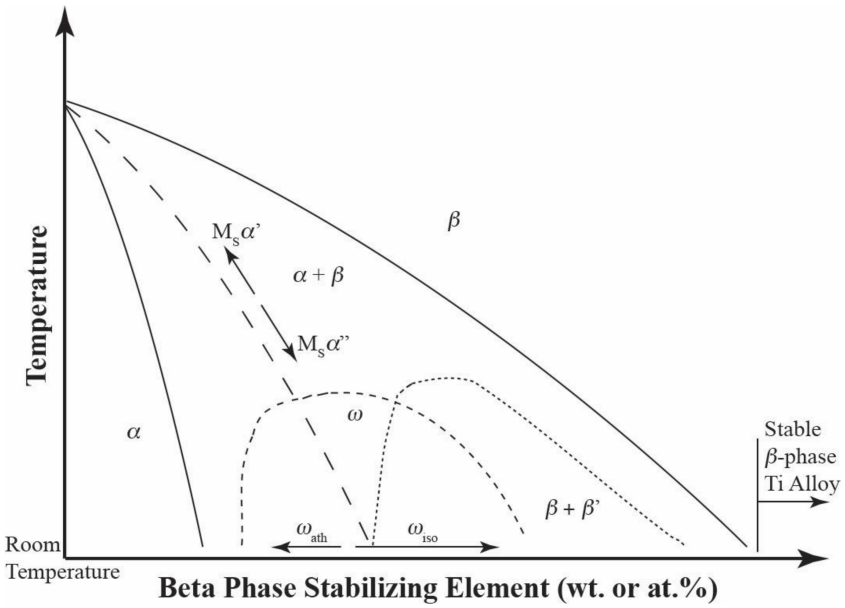

Figure 2.1: An isomorphous Ti-(β-stabilizer) phase diagram, copied from source [36]. Stable HCP α and BCC β-fields are present, as well as metastable α', α" and ω-phases.

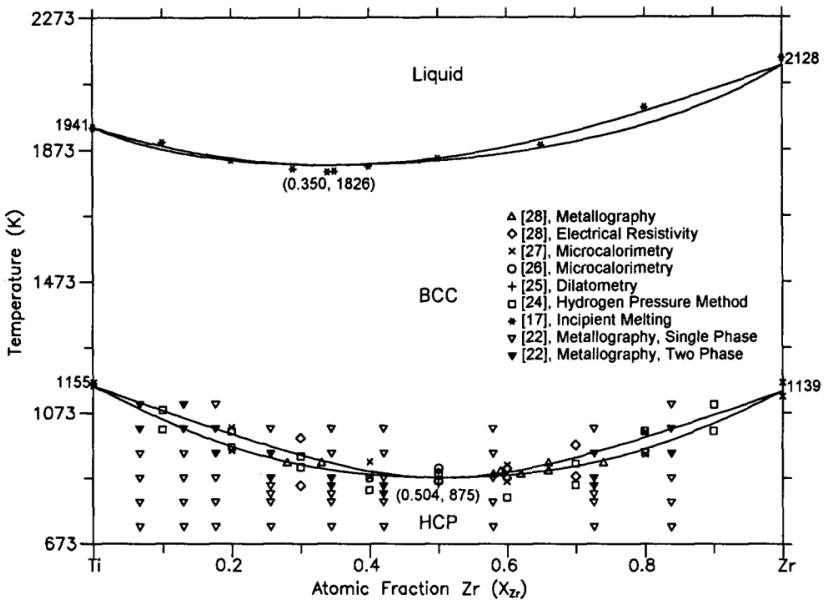

FIGURE 2.2: Computed Ti-Zr phase diagram, copied from source [26]. All present phases exhibit complete solubility.

which should be multiplied by the mass fraction of that element. Then, the sum of those products is the Mo-eq. Usually, a value of 10 distinguishes metastable β-(Mo-eq. < 10) from stable β-alloys (Mo-eq. > 10). The most commonly used equation was proposed by Molchanova: [48, 13]:

$$\begin{aligned}(Mo-Eq.)_{Molchanova} = \\ 1 \cdot Mo[wt.\%] + 0.2 \cdot Ta[wt.\%] + 0.28 \cdot Nb[wt.\%] + 0.4 \cdot W[wt.\%] \\ + 0.67 \cdot V[wt.\%] + 1.25 \cdot Cr[wt.\%] + 1.25 \cdot Ni[wt.\%] \\ + 1.7 \cdot Mn[wt.\%] + 1.7 \cdot Co[wt.\%] + 2.5 \cdot Fe[wt.\%]\end{aligned} \tag{2.1}$$

2.1.3 The Ti-Nb-Zr system

The role of zirconium in the ternary Ti-Nb-Zr system is still subject of discussion. Often, zirconium is considered as a neutral element with regard to the β-transus temperature [36]. However, in the Ti-Nb-Zr system, both Nb and Zr work as a β-stabilizer, and the stabilizing effect of Zr depends on the Nb content [1, 76]. Hence, Mehjabeen et al. found that ignoring the influence of Zr, which is the case in equation 2.1, leads to inconsistent results [45]. Consequently, they formulated an expression that is specifically focused on the Ti-Nb-Zr system:

$$(Mo-Eq.)_{Ti-Nb-Zr} = 0.238 \cdot Nb[wt.\%] + 0.11 \cdot Zr[wt.\%] + 0.97 \tag{2.2}$$

Equation 2.2 is based on experimental observations of Ti-Nb-Zr-alloys from multiple publications, and the authors validated the expression on other compositions. The alloy compositions used for this thesis lie within the range of compositions that

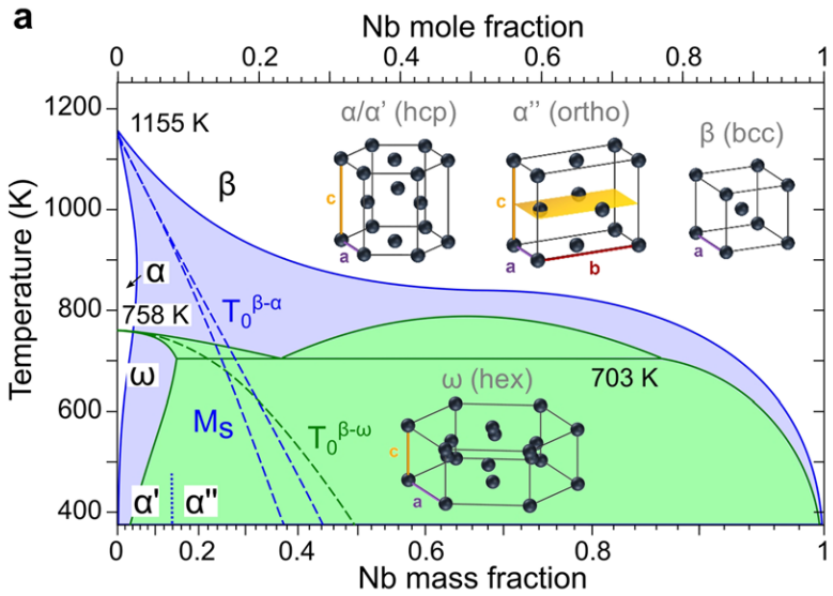

Figure 2.3: Ti-Nb phase diagram, copied from source [8]. The blue diagram represents thermodynamic equilibrium, while green includes metastable phases.

Mehjabeen et al. considered. Consequently, equation 2.2 should be applicable to calculate Mo-eq. of the alloy compositions used in this thesis.

Not only does Zr-addition inhibit the formation of α' and α"-phase upon quenching, it also prevents the formation of athermal ω-phase [35, 52, 76]. In fact, Pang et al. found that, while athermal ω-formation was supressed, zirconium did not prevent or influence isothermal precipitation of ω-phase.

2.2 High-Pressure Torsion

This section of the literature review is dedicated to high-pressure torsion (HPT). The first part explains the concept of severe plastic deformation, of which HPT is a prime example. Then, a brief summary introduces its working principles, benefits and drawbacks of HPT. A final part reviews the effects of HPT on the material structure and, consequently, (relevant) material properties.

2.2.1 Severe Plastic Deformation

Severe plastic deformation defines a collection of deformation processes, that introduce large plastic strains [17]. Doing so, they aim to strengthen crystalline materials through grain size refinement. Even though a large number of SPD processes exist, this discussion will be limited to HPT, because it is the only SPD method used in this work.

2.2.2 HPT - Working principle, benefits and drawbacks

In HPT, two anvils compress a disk-shaped sample with high force [19]. The resulting high pressure both prevents slippage between the anvils and the sample, and helps prevent failure of the sample under the applied deformation [56, 66]. One of the anvils -the lower one, in this work- rotates to deform the sample. The torsion induces in a shear strain in the sample, which is uniformly distributed through the sample thickness, and can be quantified using the following equation:

$$\gamma = \frac{2 \cdot \pi \cdot n}{t} \cdot r \tag{2.3}$$

Where:

- n is the number of revolutions
- t the sample thickness
- r the radial distance, i.e. the distance from the sample center

This axisymmetric strain distribution theoretically results in no shear strain at the center of the disk, and increasing strain towards the edges. Careful experiments evidenced that there is no deformation microstructure in the sample center and an increasingly heavily deformed structure at larger radial distances [70].

Thickness reduction during the HPT process must be considered, especially in anvil designs that allow material to flow out [67, 19]. Such anvils were used in this work, hence the processing parameters are reported as number of revolutions instead.

Compared to other (shear-type) SPD methods, HPT offers several advantages. The summary below is based on points raised by Pippan et al. [55, 56]:

- Large strains can be applied, as any large number of rotations should be possible using the same setup.
- The applied strain is continuous, in contrast to methods such as equal channel angular pressing, where a discreet number of passes needs to be used.
- The large compressive stress allows to deform usually brittle materials, such as various glasses [14].
- Torque can be measured during deformation, which allows to record strengthening behaviour, and to monitor the process, for example to discover whether slip happens.

However, HPT has some drawbacks, primarily the relatively limited sample size. Upscaling the process has a few practical limits: first, both the applied force and torque requirements increase sharply with increasing radius [55]. Second, the heat that is generated from deforming the sample becomes large. Another concern may be the inhomogeneous strain: as visible in equation 2.3, the shear strain depends on the radius. This may cause non-uniform material properties, which is not desirable for industrial applications [19].

Several HPT-based processes try to overcome some of these drawbacks mentioned above [18]. Examples are: ring-HPT, where a ring- or tube-shaped sample is used instead of a disk [25]. Then, the hollow center eliminates the strain inhomogeneity, and larger diameters are possible. Another approach uses strips, that are pressed into a grooved anvil, which subsequently slides over the strip to induce shear strain [21].

2.2.3 HPT - Material structure and properties

The structure development during SPD at low homologous temperature results from two concurrent microstructural processes [56]. Specifically, processes that fragment the grains -leading to a grain size decrease- compete with restoring processes. At a certain, large strain level, an equilibrium between both processes exists, such that the grain size distribution does not change. In other words, the process enters a steady state, where fragmentation is balanced with coarsening processes.

To illustrate the steady state, consider two cases, where the initial microstructure is either coarse-grained, or nanocrystalline [56]. In both cases, the mean grain size approaches the same value upon extended deformation [42, 71]. The following paragraphs, however, only consider the "top-down" approach, where the initial microstructure is coarse-grained and the application of HPT introduces grain size refinement [17].

HPT - Grain Fragmentation

The strain-induced grain fragmentation occurs through a mechanism similar to those responsible for strain hardening and grain size reduction in regular plastic deformation techniques [56]. The following considers the most simple case, i.e. FCC materials with high stacking fault energy, where no twinning deformation occurs and multiple slip systems are available [10]. There, generation of dislocations and their subsequent movement on glide planes accommodate the imposed deformation. The dislocations then pile up at the grain boundary, or concentrate within the grain to subdivide the grain into a structure of cell blocks and dislocation cells. If mechanical failure is prevented, as is the case in SPD methods, this process continues up to a point where the misorientation between these structural elements increases to such a degree that they form grain boundaries. In fact, a high amount of high-angle grain boundaries is a characteristic feature of microstructures of SPD materials [66]. The grain subdivision process explained in this paragraph is schematically illustrated in Figure 2.4.

The β-Ti-alloys studied here, however, consist of single-phase body-centered cubic (BCC) structure during HPT processing. Since plasticity in BCC metals can occur through both screw and edge dislocations on multiple possible sets of glide planes -{1 1 0}, {1 1 2}, and {1 2 3}-, the deformation processes are not as straightforward as those explained above [10]. Still, the formation of different dislocation-based intragranular boundaries have been observed, and they cause subdivision through a similar, hierarchical process.

HPT - Grain Size Restoration

As mentioned earlier, at steady state, there should be a process that occurs simultaneously with fragmentation, and stabilizes the grain size, by promoting some sort of coarsening. Based on both theoretical arguments and experimental observations, grain boundary migration (GBM) seems to be the dominant mechanism [56, 10]. In this process, the grain boundary moves in a direction that is perpendicular to the strain direction, as visible in Figure 2.5. The migration is accommodated by movement of disconnections in the grain boundary.

GBM then explains why grains are not excessively elongated in the strain direction [56]. Generally, GBM is promoted by increasing temperature [59]. This finding therefore clarifies why grain size is smaller when deformation occurs at colder temperatures.

The effect of alloying on grain size can be explained this way as well: increased alloying element content lowers grain boundary mobility, due to solute drag, which in turn should then result in a more pronounced grain fragmentation, which corresponds well to observations [56].

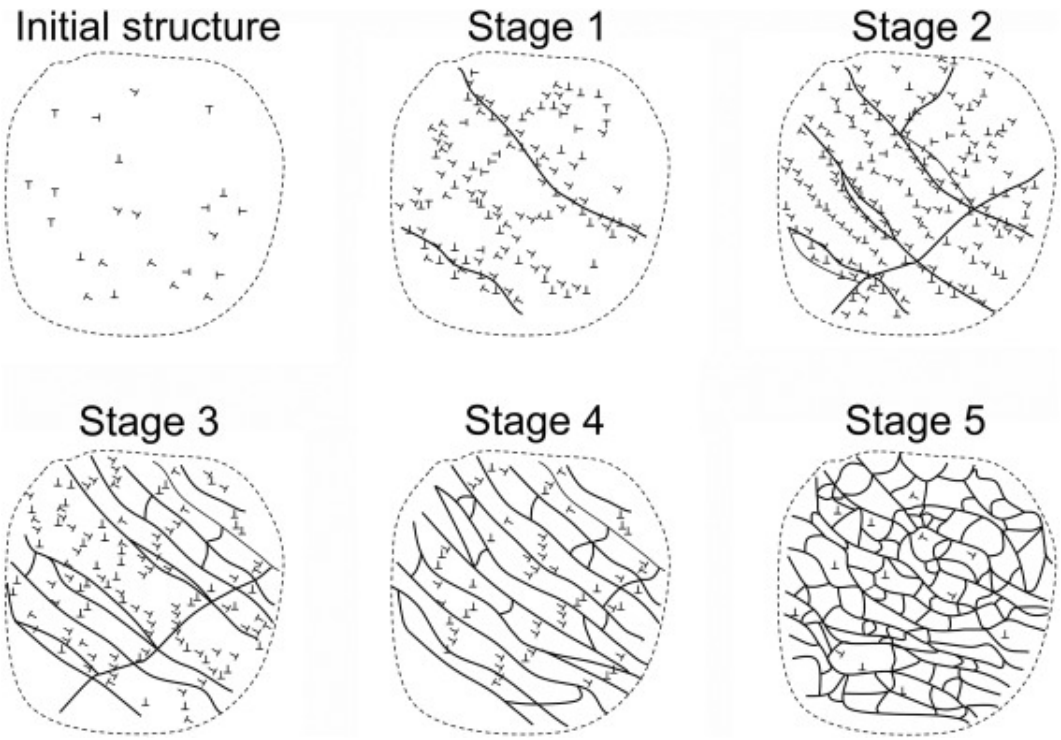

FIGURE 2.4: The process of grain subdivision upon deformation of FCC materials with high stacking fault energy, copied from Cao et al. [10]. In stages 1-4, increasing degree of deformation causes dislocations to concentrate and form cellular structures, whose misorientation gradually increases. Eventually, in steady state, a somewhat equiaxed structure is formed with high angle boundaries, stage 5.

Hardening by HPT

The grain size refinement that follows from SPD processes causes hardening in these materials. Initially, the increase in yield stress obeys the Hall-Petch relationship, stating [24, 54, 66]:

$$\sigma_y = \sigma_{y,0} + \frac{K}{\sqrt{d}} \tag{2.4}$$

Where:

- σ_y is yield stress (original, coarse-grained: subscript 0)
- d is grain size
- K is a constant

However, in ultafine-grained (UFG) polycrystals, below a certain grain size, the increase in yield stress is less significant than the value predicted from the Hall-Petch law [12, 46]. This breakdown can be attributed to the Hall-Petch theory's reliance on large dislocation pile-ups at grain boundaries, which cannot be realized in small grains.

2.3 Anneal hardening

In UFG and nanocrystalline (NC) materials, annealing-induced hardening is often observed [60]. In other words, upon annealing at low to moderate temperature -up to about 0.48 x T_{melt}-, the hardness increases relative to its pre-annealing state [22]. Literature not only reports enhanced hardness, but also a lower elongation until failure in these materials. Both findings are opposite of those in coarser-grained materials, where annealing improves ductility, at the expense of hardness [22]. An even more remarkable observation is that, upon deformation of such anneal-hardened UFG or NC materials, the ductility partially or fully recovers, while hardness slightly decreases [30].

The origin of anneal hardening seems to lie in two processes, simultaneously occuring during low-temperature annealing [60, 22]. First, glide of mobile dislocations

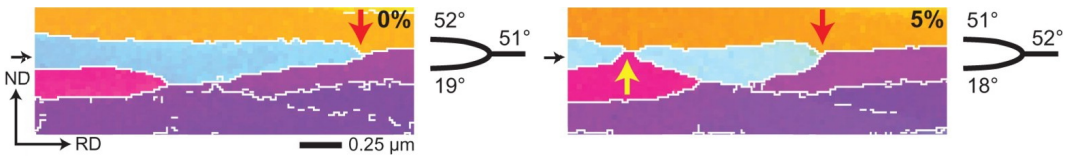

Figure 2.5: Observed grain boundary migration in cold-rolled Al, copied from Yu et al. [74]: both pictures show orientation maps. The left-hand map shows the initial state, where the plate has been cold-rolled to a trues strain of 4. Then, the right-hand side shows the same region with an additional thickness reduction of 5 %. The red arrow indicates the movement of a triple junction, while the yellow arrow shows grain boundary motion perpendicular to the rolling direction (RD).

in the grain interior is thermally activated upon annealing. Consequently, these dislocations either annihilate, get absorbed into the grain boundary, or coalesce to form low-angle grain-boundaries [23]. As a result, the availability of dislocations that may facilitate plasticity decreases, which is reflected in literature, observing a dislocation density decrease during annealing [40].

Second, grain boundaries generated by SPD, as explained above, contain a large number of defects, and are often considered non-equilibrium grain boundaries. Upon grain size refinement, the nature of dislocation generation shifts from intragrain sources, such as Frank-Read sources, to grain boundary-based dislocation emission. The latter relies on defects such as ledges to nucleate dislocations [68]. Annealing induces an overall decrease in excess grain boundary energy, meaning the density of available dislocation nucleation sites in grain boundaries diminishes, which increases the nucleation energy barrier. In combination, these two effects inhibit dislocation-based plasticity upon deformation of anneal-hardened materials, since fewer active dislocations or nucleation sites are available after the annealing treatment [40].

In principle, anneal hardening only considers the two effects described above [60, 22]. Still, in practice, these effects can be difficult to isolate, as other strengthening mechanisms may occur simultaneously. For example, solute segregation or precipitation hardening may occur in alloys [3]. In addition, the effect of anneal hardening strongly depends on the processing history of the UFG or NC material. Therefore, the influence of, for example, grain size is difficult to investigate, because a significant change in grain size requires alloying or a change in processing parameters [60].

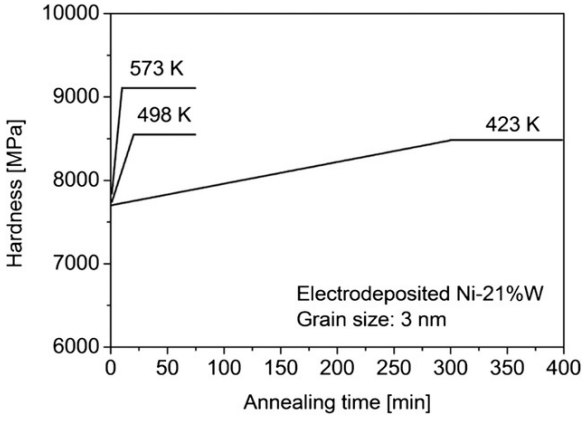

(A) Annealing time influence on hardness in electrodeposited Ni-21%W at different temperatures. Figure copied from J. Gubicza, using data from Rupert et al. [22, 61].

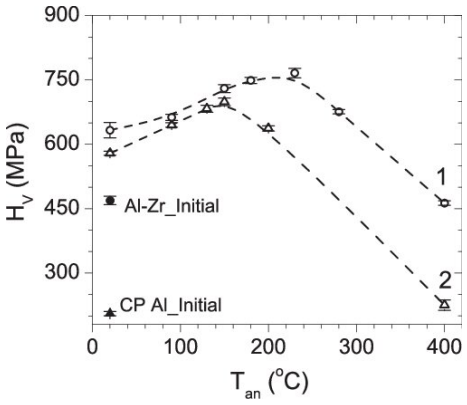

(B) Hardening of commercially pure (CP) aluminium and Al-0.4Zr (wt.%), demonstrating the effect of annealing temperature (using 1 h time) on Vickers hardness. Figure copied from Latynina et al., using data from Mavlyutov et al. as well [44, 39].

FIGURE 2.6: Representative figures for influence of annealing time (2.6a) and temperature (2.6b) on anneal-hardening behaviour.

The time scale to reach a saturated annealing-induced hardness should be relatively short, as can be seen in Figure 2.6a [60, 22]. For example, in many materials, an annealing time up to 1 h, at temperature lower than 800 K (527 °C), leads to a pronounced hardening, up to 25 % [22]. Based on these observations, Renk and Pippan [60] even argue that hardening over a long time period may indicate that other mechanisms are active as well, such as precipitation.

Usually, the hardness increase peaks at a certain temperature, above which it decreases again, as can be seen in Figure 2.6b [22, 39]. At those temperatures, softening occurs due to microstructural coarsening, by grain growth [60].

Chapter 3

Methodology

Figure 3.1 schematically displays the approach used in this thesis. Each row represents a different stage in the process, and each stage consists of different steps. The paragraphs below chronologically detail each steps. Figure 3.1 does not include characterization methods which were not carried out on each sample, i.e. transmission electron microscopy (TEM) and energy dispersive X-ray spectroscopy (EDX).

3.1 Alloy Synthesis

The alloy synthesis consisted of arc-melting commercial Ti-30at.%Nb alloy with pure Zr (Zr702, 99.2% purity) into button ingots in 0.8 atm argon atmosphere. Remelting the ingots five times aimed to ensure chemical homogeneity in the samples. Cylinders with 8 mm diameter were electrical discharge machined out of the button

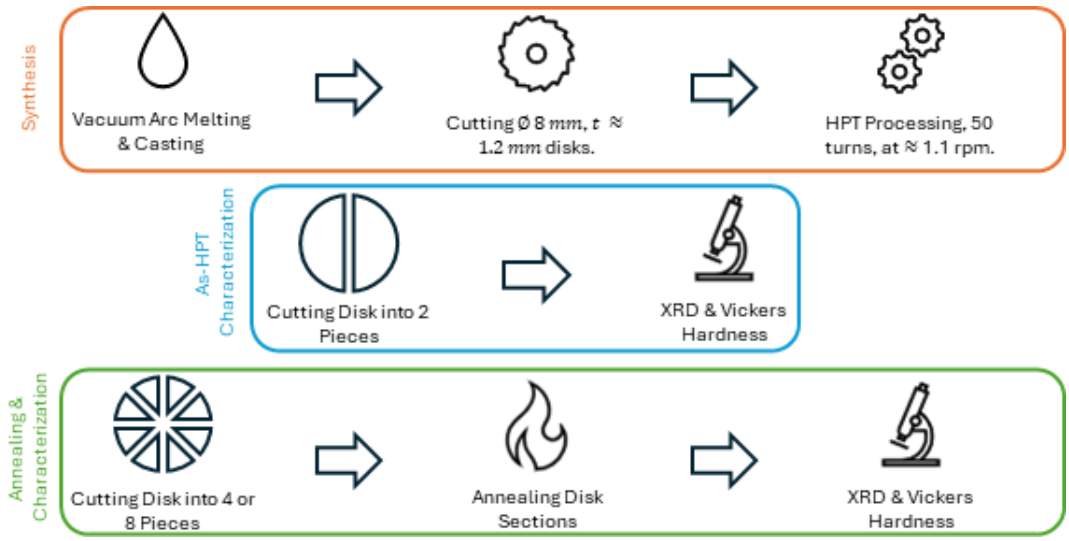

FIGURE 3.1: Experimental approach used in this work. Rows represent different stages, each consisting of sequential steps.

ingots. Finally, a diamond disk cutter was used to cut HPT disks with 0.8 to 1.2 mm thickness from the cylinders.

The alloy compositions used in this work are listed below, in Table 3.1. The leftmost column defines how the composition will be referred to in this work.

Table 3.1: Alloy compositions used throughout this work.

Name	Ti [at.%]	Nb [at.%]	Zr [at.%]	Ti [wt.%]	Nb [wt.%]	Zr [wt.%]	Mo-Eq. using eq. 2.2
5 % Zr	66.8	28.2	5.0	51.0	41.7	7.3	11.7
10 % Zr	63.3	26.7	10.0	47.2	38.6	14.2	11.8
25 % Zr	52.8	22.2	25.0	36.7	30.1	33.2	11.7

3.2 High-Pressure Torsion

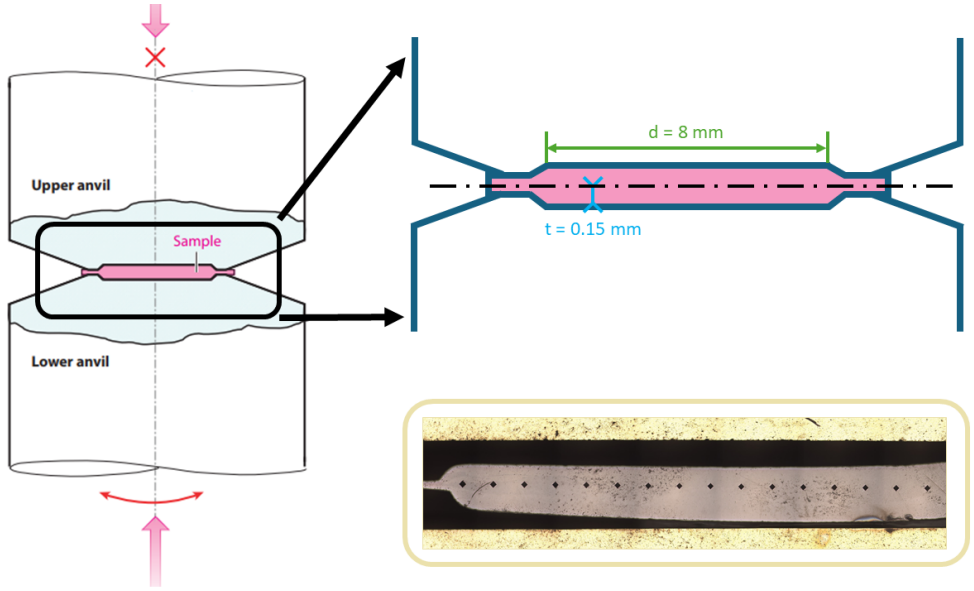

Figure 3.2: Schematic of the HPT setup: quasi-constrained anvils with a compressed sample inside, after source [56]. Inset: picture of half a HPT-processed sample with Vickers hardness indents in brass holder.

Sand-blasted, disk-shaped Ti-Nb-Zr samples mentioned previously were used as starting material. The disks were compressed in sand-blasted, modified quasi-constrained type anvils (illustrated in Figure 3.2), with a diameter (d) of 8 mm and groove thickness (t) of 0.15 mm [56]. Each anvil set was used to deform two disks, before re-machining the anvil surface. Between processing those two samples, the anvil surface was sand-blasted again to avoid slippage.

The HPT device operated at a rotational speed of 1 rpm, at maximal compressive force (390 kN), equivalent to a compressive pressure of about 7 GPa. 50 revolutions were performed at room temperature. The final sample thickness was around 0.50 mm. Following HPT, the samples were cut in half through the thickness direction using a diamond-wire cutter for further analysis steps. Figure 3.3a shows an HPT disk cut in half.

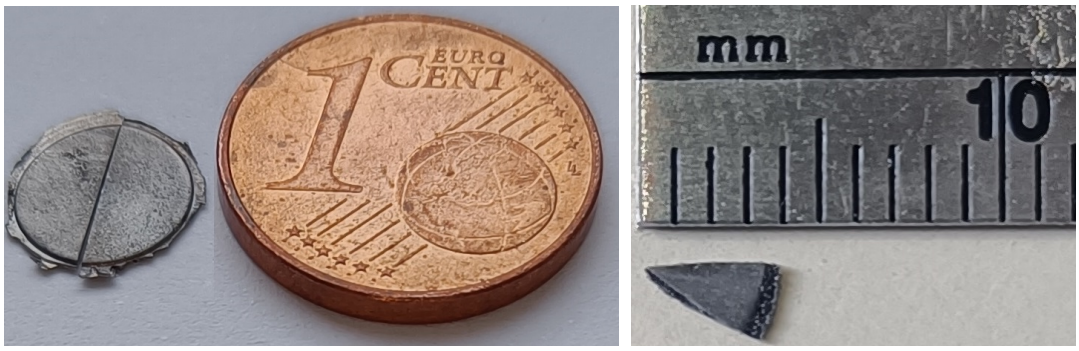

(A) HPT disk, already cut in half. (B) An $^1/_8$th section of an HPT disk.

FIGURE 3.3: HPT disk and $^1/_8$th section, with 1-eurocent coin and ruler, for scale.

3.3 X-Ray Diffraction

X-Ray Diffraction (XRD) was performed on selected as-HPT- and annealed samples, in a Bruker D8 diffractometer with Bragg-Brantano geometry using Co K_α radiation (λ= 0.179 nm [2]). Two diffractograms were measured for each sample, using the measurement parameters from Table 3.2. A broad 2θ-range was used to include sufficient peaks from each phase, while the narrow range allowed to inspect the $(1\ 1\ 0)_\beta$ -peak in detail. The 2θ-Intensity output was exported as a text file, and was further processed using a Python v3.10 script, developed for this analysis.

The Python script used following steps to process the XRD data: background-subtraction, peak-fitting, smoothing and plotting. First, the background subtraction

TABLE 3.2: Parameters for XRD measurements.

Type	Sample Dimensions	2θ [°]	2θ Step Size [°]	Time per Step [s]	Sample Rotation Speed [rpm]	Incident Beam Slit Width [mm]	Radiation Source
Long	down to $^1/_4$	20-120	0.05	2	15	0.6	Co
Long	$^1/_8$	20-120	0.05	4	15	1	Co
Short	all	38-48	0.01	3.5	15	both	Co

used the pybaselines library [15]. Broad-type measurements used the range independent algoritm, while narrow-type measurements used constant background value. Next, the $(1\ 1\ 0)_\beta$ -peak was fitted with the Pseudo-Voigt model using the lmfit library, to determine the full width at half maximum (FWHM) [50]. For potting, a 4-point moving average function (numpy library) was used to smoothen the background-subtracted spectra [27]. Results were visualized on plots using matplotlib [31].

3.4 Vickers Hardness

Hardness measurements were performed on polished sample cross-section along radial direction, using a ZwickRoell Durascan 70 device. Figure 3.2 shows an indented sample. The device applied a load of 0.5 kgf during 15 s. The diagonal lengths were measured using an algorithm provided by the device manufacturer, though manual correction was sometimes necessary. The spacing between indents was 250 µm. Considering the mean diagonal length was below 50 µm in most cases, the minimum spacing requirement of $5 \cdot d_{mean}$ was satisfied [32].

3.5 Annealing

As explained in Figure 3.1, annealing was performed on $^1/_4$ or $^1/_8$ disk sections, using a Heraeus resistance-heated air furnace. These HPT disk sections were wrapped in annealing foil, to slow down oxidation. Annealing temperatures were 100, 200, ..., 600 °C, and 150 and 350 °C. Table 3.3 lists the combinations of annealing temperature and times that were used. The selection is based on results from Voelker et al. [69], and considers the time and instrument availability.

Table 3.3: Annealing temperature and time combinations used in this work. Numbers in cells represent compositions, e.g. 5 refers to a 5 % Zr sample, and A represents all compositions.

		Temperature [°C]							
		100	150	200	300	350	400	500	600
Time [h]	0.25	-	10	-	A	A	A	-	-
	0.5	A	10	A	A	A	A	A	A
	0.75	-	10	-	A	A	A	-	-
	1	-	10	-	A	A	A	-	-
	1.25	-	10	-	5	5	5	-	-
	1.5	-	10	-	5	5	5	-	-
	2	-	10	-	A	A	5, 10	-	-
	4	5	10	5	A	A	5, 10	5	5

3.6 Hardening Kinetics Analysis

The analysis of hardening kinetics is briefly explained here. The method follows the approach described by Rupert et al. [61]. First, the linear hardening constant k is calculated. For simplicity, this work will only consider the hardness change at 30 min, although Rupert et al. use the slope of ΔH(t[min.])[GPa]. However, in this work, at temperature below 300 °C, an insufficient amount of datapoints are available. So, the kinetic constant k_{30}, is calculated as follows:

$$\begin{aligned} H_{ann.} - H_{as-HPT} &= \Delta H[GPa] \\ &= \frac{\Delta H[HV0.5] \cdot\ g}{10^3} \\ &= k \cdot\ t \\ &= k_{30} \cdot\ 30[min]. \end{aligned}$$

$$\implies k_{30}[{}^{GPa}/_{min.}] = \frac{\Delta H[HV0.5] \cdot\ g}{10^3 \cdot 30[min.]} \tag{3.1}$$

Where:

- ΔH is the hardness change compared to the as-HPT state
- t is the annealing time (set at 30 min)
- g ≈ 9.81 is the gravitational constant, which in this case is used to convert units from HV0.5 to MPa ([HV0.5] is equivalent to $[{}^{\text{kgf}}/_{\text{mm}^2}]$).

Note that this equation uses the surface area hardness, rather than the projected area hardness. It is unclear which one is used in the article by Rupert et al. [61]. Then, the Arrhenius equation is adjusted to the hardening constant as:

$$k_{30} = A[{}^{GPa}/_{min.}] \cdot\ exp\left(\frac{Q[{}^{J}/_{mol}]}{R[{}^{J}/_{K \cdot mol}] \cdot\ T[K]}\right) \tag{3.2}$$

$$= A[{}^{GPa}/_{min.}] \cdot\ exp\left(\frac{Q[J]}{k_B[{}^{J}/_{K}] \cdot\ T[K]}\right) \tag{3.3}$$

Where:

- A is a pre-exponential constant with same units as k_{30}
- Q the activation energy, which can be normalized to moles, by using the ideal gas constant $R \approx 8.31\ J \cdot K^{-1} \cdot mol^{-1}$ instead of the Boltzmann constant $k_B \approx 1.38 \cdot 10^{-23}\ J \cdot K^{-1}$
- T is the annealing temperature [K]

3.7 Energy Dispersive X-Ray Spectroscopy

Energy-dispersive x-ray spectroscopy (EDX) was carried out on a Tescan - MAGNA scanning electron microscope, using an acceleration voltage of 30 kV and current of 300 pA. L-emission lines were used to evaluate Nb and Zr content, because their intensity was higher than the corresponding K-emission lines. Sets of 12 measurements were performed on annealed samples at different radii, usually at 2, 3 and 4 mm, as indicated on Figure 3.4. Two 25 % Zr as-cast samples were mapped.

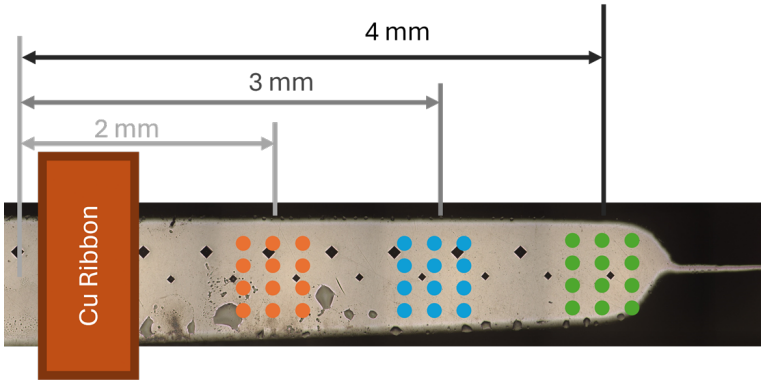

Figure 3.4: Setup for EDX composition measurements: 3 sets of 12 point measurements at different radial distances.

3.8 Differential Scanning Calorimetry

Differential Scanning Calorimetry (DSC) was performed using a Mettler Toledo DSC 3+ devide. The heat flow in two heating-cooling cycles was recorded. Each cycle consisted of a 30 min isothermal hold at 50 °C, to equilibrate the device, with subsequent heating at 10 $K \cdot min^{-1}$ up to 600 °C, followed by cooling at -50 $K \cdot min^{-1}$ to the starting temperature of 50 °C.

3.9 Note on plots

The plots in this thesis will use $1 \cdot s$ as length for either side of errorbars, such that combined length of bottom top errorbars is $2 \cdot s$, with s the sample standard deviation. The errorbars corresponding to $(1\ 1\ 0)_\beta$ FWHM considers the error on the Pseudo-Gaussian peak fitting.

For annealed samples, the estimated standard deviation of the difference in mean hardness between as-cast and annealed state, ΔH, was calculated according to the following formula [49]:

$$s_{\Delta H} = \sqrt{\frac{(n_{HPT} - 1) \cdot s_{HPT}^2 + (n_{ann.} - 1) \cdot s_{ann.}^2 +}{n_{HPT} + n_{ann.} - 2}} \tag{3.4}$$

Where:

- ΔH is the difference in mean hardness between as-cast and annealed state
- subscript *HPT* refers to hardness measurements on the as-HPT sample
- subscript *ann.* refers to hardness measurements on the annealed sampl

Then, $s_{\Delta H}$ best estimates the standard deviation of the mean hardness difference between as-HPT and annealed samples.

Chapter 4

Results

The first part of this chapter presents the observed chemical composition and its spatial distribution, and their correlation with hardness and XRD data. Afterwards, the hardening by HPT and subsequent annealing in the 5 % Zr composition is discussed representatively, because the measured trends are similar to the other two samples. A final section compares results for all three compositions.

4.1 Chemical Composition

Certain hardness measurements presented further in this chapter show large scatter. To determine the cause, those measurements were repeated after grinding the plastically deformed zone away. Again, the scatter on hardness values was large. Then, sample compositions were measured using EDX, as described in section 3.7. Those results showed a significant lack of solute mixing on as-cast samples. The following paragraphs summarize the extent of composition fluctuation and its effect on hardness and XRD results.

4.1.1 Composition Effect on Hardness

The investigated as-cast 25 % Zr sample was not sufficiently mixed during arc-melting, as evidenced by Figure 4.1. The EDX composition map (4.1a) indicates two distinct regions: the dark-colored one is depleted in zirconium, its composition is nearly identical to the Ti-45wt.%Nb feedstock alloy. The other, bright-colored region has an average Zr-content around 25 at.%. The gradient between these two regions is extremely steep, so that almost no alloy with intermediate composition exists.

The X-Ray diffractogram (4.1b) of the as-cast 25 % Zr sample supports the findings above. The strongest reflection is the $(1\ 1\ 0)_\beta$ -peak, between 43° and 46°. The upper inset reveals a peak-split, and the peak with higher 2θ corresponds well to lattice parameters of Ti-30at.%Nb [64]. Considering the atomic radius is larger for zirconium than for titanium or niobium, the left peak (at 44.2°) can be attributed to the region containing zirconium [52]. The second, smaller inset reveals a similar double $(220)_\beta$-peak, between 95° and 102°.

As-cast hardness

The non-homogeneous zirconium distribution throughout as-cast samples may affect hardness as well. This can be appreciated for both 10% and 25 % Zr as-cast disks on the countour plots of Figure 4.2a and Figure 4.2b, respectively. On the 10 % sample, measured hardness values range from 235 up to 270 HV0.5, and most of the bulk values lie between 0 and 255 HV0.5 and values at the edges seem slightly higher. The 25 % Zr sample, shows very low hardness at the top edge, going down to 170 HV0.5. This decrease can probably be attributed to alignment issues, meaning the sample surface is not completely perpendicular to the indentation direction. Then, the bulk hardness seems to range between 5 and 285 HV0.5.

As-HPT Hardness

Figure 4.3 plots as-HPT hardness against measured Zr-content. In this case, EDX measurements used annealed samples, not as-HPT samples. Still, the spatial distribution of alloying elements should remain similar to as-HPT state, because of low diffusion coefficient values [47]. In Figure 4.3, the influence of Zr-content on hardness is clear: a higher mean Zr-content results in higher hardness.

Figure 4.3 indicates that a inhomogeneous Zr-distribution, visible as horizontal errorbars, results in inhomogeneous hardness, vertical errorbars. Note that, in as-HPT samples, the hardness profile is not uniform, similar to publications on other β-stabilized Ti alloys [4, 73, 33]. Still, compared to the EDX map of as-cast sample (Fig. 4.1a), HPT seems to significantly improve mixing in 25 % Zr samples. To summarize, even after remelting and flipping the button ingot five times during arc-melting, the spatial distribution of alloying element was not perfectly homogeneous.

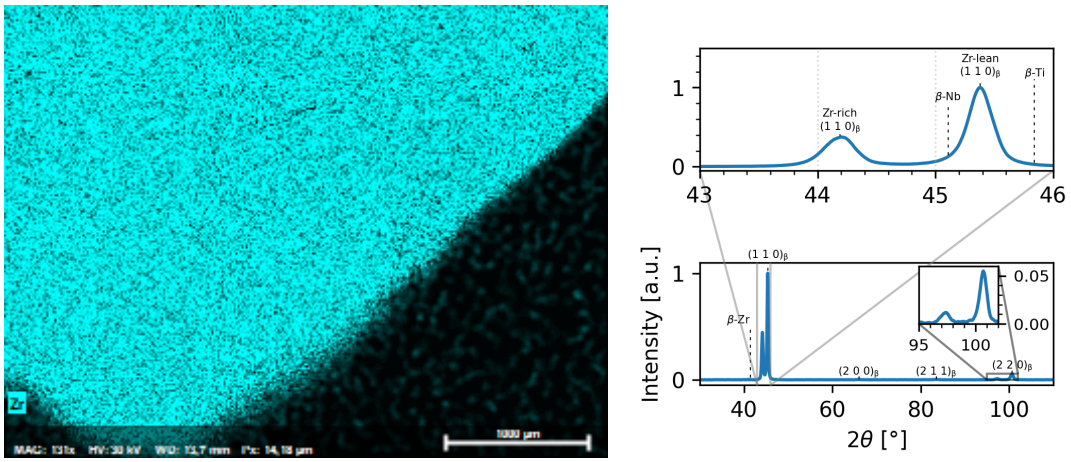

(A) EDX composition map: Zr distribution in an as-cast 25 % Zr sample. Maximal brightness corresponds to about 25 at.% Zr.

(B) X-Ray diffractogram, where alloy β-phase reflection peaks are indicated, as well as (calculated) $(1\ 1\ 0)_\beta$ peaks for the constituent metals: Ti, Nb and Zr.

Figure 4.1: As-cast 25 % Zr sample:

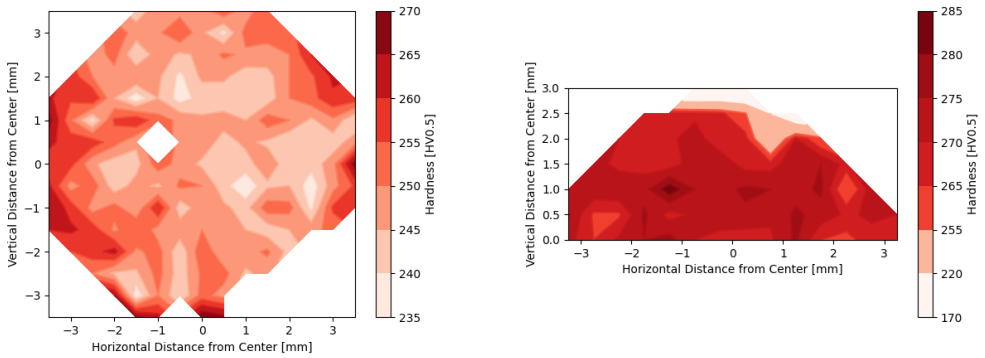

(A) 10 % Zr sample. (B) 25 % Zr sample.

FIGURE 4.2: Vickers hardness of as-cast samples, indented on disk surface:

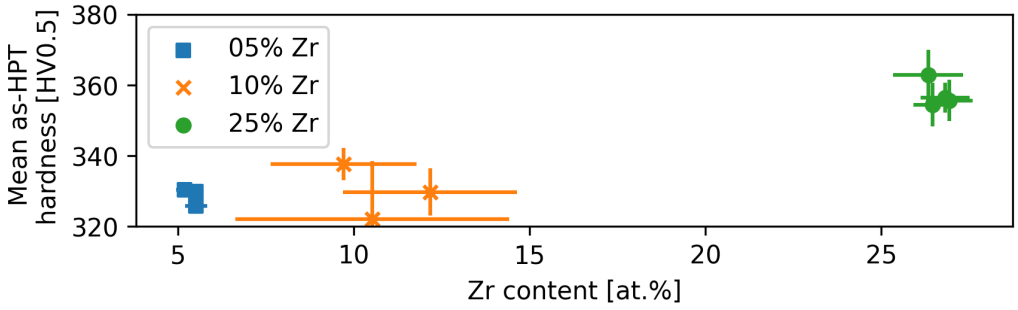

FIGURE 4.3: Correlation between Vickers hardness and Zr-content in as-HPT samples.

As a result, hardness may vary locally. Still, as best illustrated by 10 % Zr samples in Fig. 4.3, the hardness fluctuations stay limited.

4.1.2 Composition Effect on XRD

Comparison between as-cast and as-HPT diffractograms further evidences the demixing observed above: Figure 4.4 shows that peak splitting does not occur for the as-HPT sample. However, the as-HPT peak is significantly broader, which still may be due to compositional inhomogeneity, but is also affected by the small grain size and large lattice defect density in as-HPT specimens.

As expected from XRD results above, Figure 4.5 shows that Zr-content influences the position of the $(1\ 1\ 0)_\beta$ peak. Indeed, despite the large errorbars on the single 10 % Zr sample -peak positions were not recorded for all samples-, the peak reflections shift to lower 2θ values for Zr-rich compositions. The slope quantifies the effect of zirconium additions on the peak position: an addition of 1 at.% Zr decreases the peak center position by about $44.5 \cdot 10^{-3}\ \frac{deg.}{at.\%}$, which is in the same order of

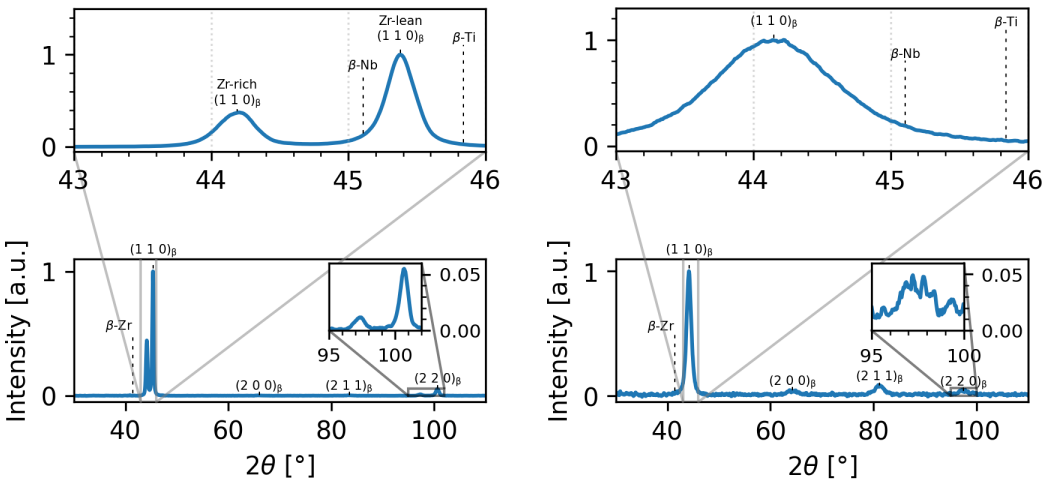

(A) As-cast (Fig. 4.1a) (B) As-HPT.

Figure 4.4: 25 % Zr sample X-Ray diffractograms, where β-phase reflection peaks are indicated, as well as BCC peaks of the constituent elements of the alloy.

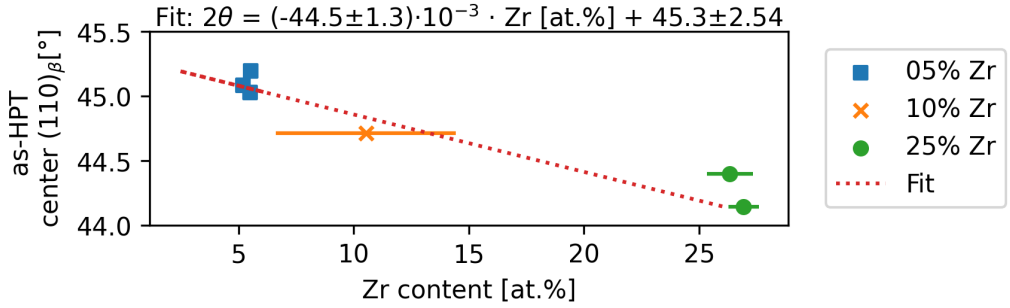

Figure 4.5: Correlation between $(1\ 1\ 0)_\beta$ peak center and Zr-content in as-HPT samples.

magnitude as results from Ji et al. ($-55.7 \cdot 10^{-3}\ \frac{deg.}{at.\%}$, in Ti-Ta-Nb-Zr high-entropy alloys, accounting for the Co radiation source used in this thesis) [34]. The large standard deviation of the composition measurement in the 10 % Zr alloy impacts the uncertainty on the intercept more strongly than the slope.

4.2 Hardening by HPT

An example of the radial hardness profile of an as-HPT sample is visible in Figure 4.6. As can be seen, the hardness distribution along the radial direction of the cross-section is uniform: the difference between the maximal and minimal hardness value is 9 HV0.5. Since there is no obvious radial dependence of hardness, the following

(and above) use the mean and standard deviation to quantify sample hardness.

Figure 4.7 (a) indicates that the mean as-cast hardness seems to increase with increasing Zr-content. That trend is even more clear in the as-HPT samples. As expected from the findings in section 4.1 above, the observed compositional fluctuations are very strongly reflected in the measured standard deviation of the as-cast samples, as can be seen on. Unfortunately, data on as-cast 5 % Zr is missing, due to time constraints.

4.2.1 HPT Effect on Hardness

Clearly, HPT causes significant material strengthening: in 10 % Zr samples, the hardness increased by 85 HV0.5, in 25 % Zr samples, it was 93 HV0.5. In fact, both are an increase of about 35 %. This percentage is lower than reported results on other β-Ti alloys, such as Ti-15Mo, Ti-45Nb and Ti-29Nb-13Ta-4.6Zr (wt.%) [73, 33, 69]. In Ti-15Mo, however, ω-phase was present, which may have been formed by high hydrostatic pressure and can enhance strength [78]. Still, Voelker et al. found an increase up to 75 % in the single-phase β-alloy Ti-45Nb (wt.%) [69].

4.2.2 HPT Effect on FWHM

HPT not only causes hardening, but also broadening of XRD peak reflections, which is highlighted by the full width at half maximum (FWHM) of the $(1\ 1\ 0)_\beta$ peak in Figure 4.7 (b). As mentioned before, the as-cast 25 % Zr diffraction pattern consists of a Zr-rich and Zr-depleted peak (see Fig. 4.1b). Hence, Figure 4.7 (b) only considers the FWHM of the $(1\ 1\ 0)_\beta$ peak centered at 45.4°, as can be seen on the rightmost graph of the same figure. In contrast, figure 4.8 confirms that no peak-splitting occurred for samples with 5 and 10 % Zr.

The HPT-induced broadening is caused by a variety of factors, mainly increased defect density, lower crystallite size and higher lattice strains [65]. In all studied compositions, HPT causes an increase of FWHM. Its magnitude seems to vary with Zr-content: they are 0.09°, 0.34° and 1.27° for 5, 10 and 25 % Zr, respectively.

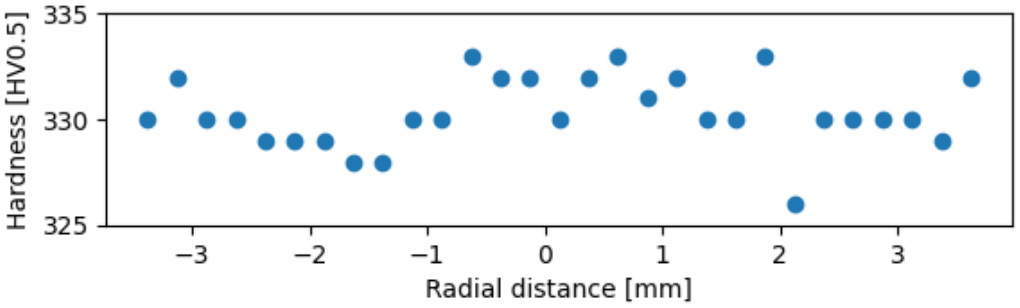

FIGURE 4.6: Vickers hardness measured on the cross-section of an as-HPT 5 % Zr sample, as function of radial distance.

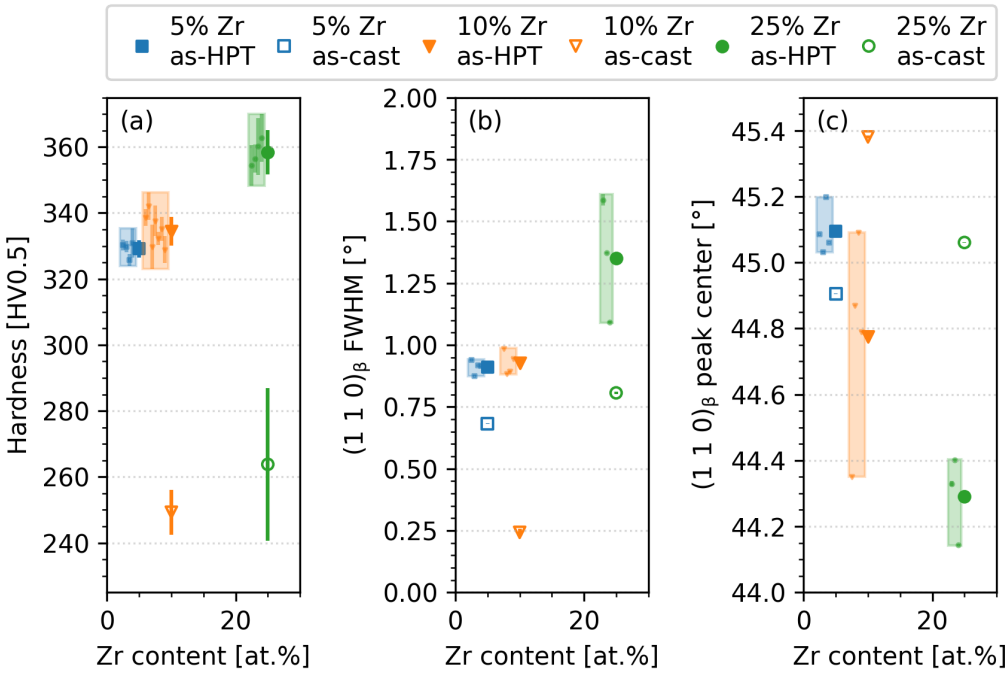

Figure 4.7: (a) Vickers hardness and $(1\ 1\ 0)_\beta$ FWHM (b) and peak center (c) for as-cast (open markers) and as-HPT (filled markers) samples. Shaded areas represent individual samples, the full-sized markers averages their data. Position on the composition-axis refers to ideal alloy composition, because alloy composition was not measured for each sample.

Moreover, increasing Zr-content results in a larger as-HPT $(1\ 1\ 0)_\beta$ FWHM. As mentioned earlier, alloying decreases equilibrium grain size, which could explain this observations [56, 16]. Similarly, no grain size measurements were performed on as-cast material, so it is unclear why the increase in FWHM for the 5% sample is rather limited. The FWHM difference between as-cast 5 and 10 % Zr samples compared to the 25 % Zr sample seems large. Perhaps, the first two have considerable compositional peak broadening, caused by chemical inhomogeneities that are observed in section 4.1.

4.2.3 HPT Effect on Peak Position

High-pressure torsion seems to have little influence on the $(1\ 1\ 0)_\beta$ peak position, shown in Figure 4.7 (c). For both 5 and 10 % Zr samples, the mean peak center of as-cast and as-HPT are closer than the distribution of as-HPT samples. In fact, there seems to be a large spread on the position of the peak center among the 10 and 25 % Zr samples. This may be linked to the larger compositional fluctuations that were observed for these alloys, in contrast to the rather similar composition between 5 % Zr samples.

Figure 4.9 plots as-HPT $(1\ 1\ 0)_\beta$ peak FWHM and peak position for the studied compositions. A higher Zr-content shifts the peak position to lower 2θ value, while its width increases. Between samples with the same composition, there only seems to be a weak, if any, correlation between the peak position and width. For example, among the 10 % Zr samples, the width seems to slightly increase with decreasing center position. Both parameters vary strongly between samples of the same composition, so more consistent data is required to investigate a possible correlation.

In summary, HPT causes significant strengthening compared to the as-cast state for all studied compositions. Not only the grain size refinement, but also the high defect density result in a significant increase in the $(1\ 1\ 0)_\beta$ peak width. The

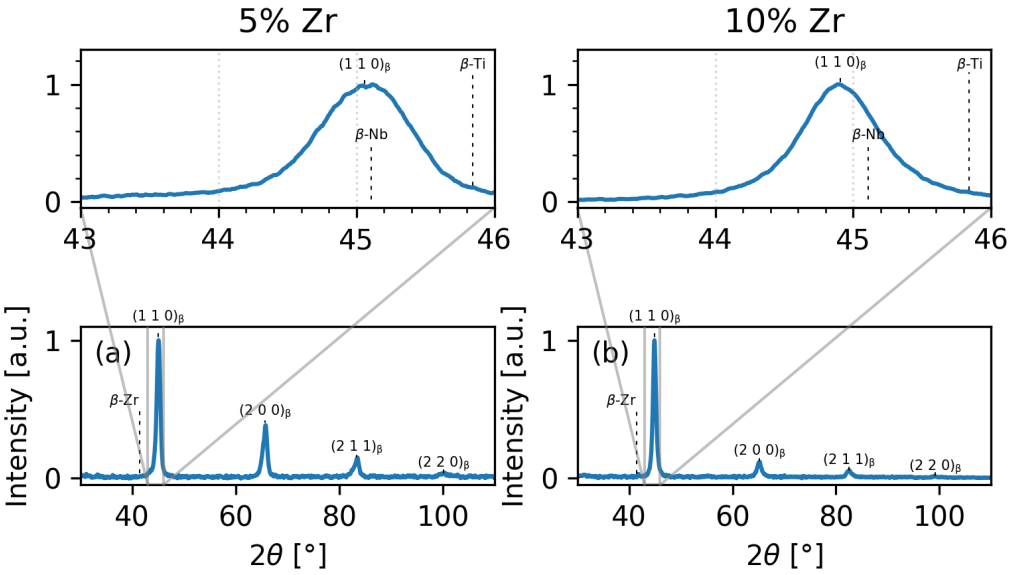

FIGURE 4.8: X-Ray diffractograms for as-cast 5 and 10 % Zr samples, where alloy β-phase reflection peaks are indicated, as well as (calculated) $(1\ 1\ 0)_\beta$ peaks for the constituent metals: Ti, Nb and Zr.

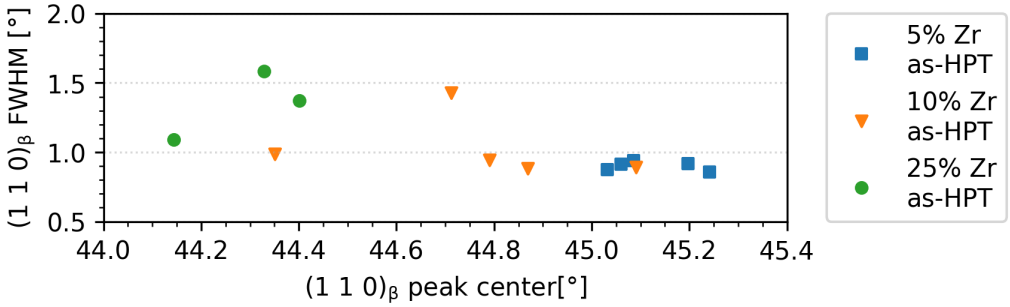

FIGURE 4.9: Center position and FWHM of the $(1\ 1\ 0)_\beta$ XRD peaks in as-HPT samples.

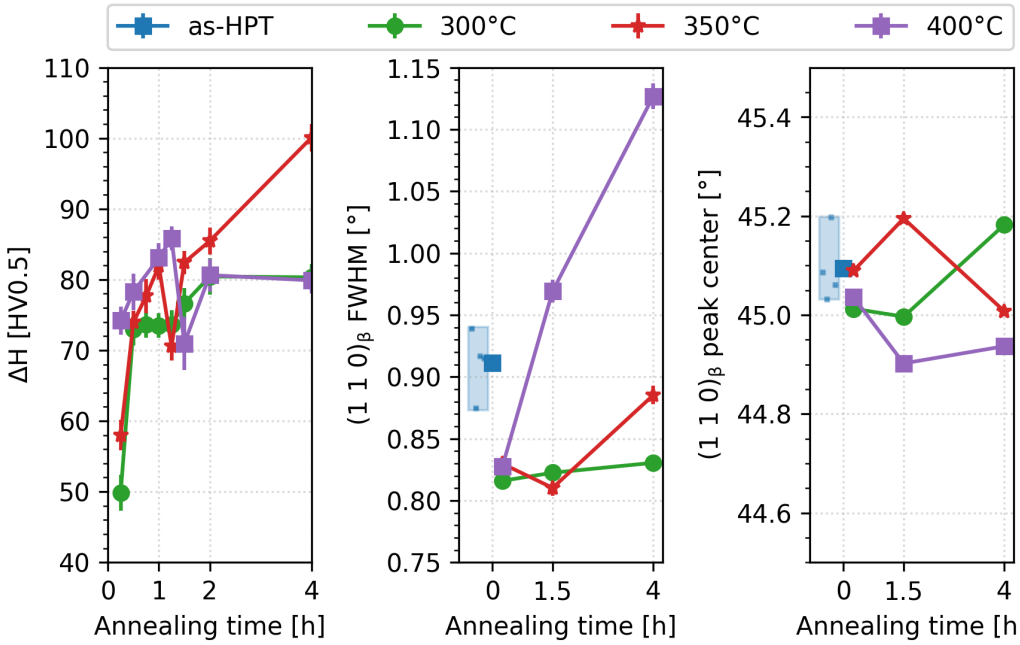

Figure 4.10: Hardness change -ΔH-, and $(1\ 1\ 0)_\beta$ peak FWHM and center of selected annealed 5 % Zr samples, as function of annealing time.

presented data does not indicate a strong effect on $(1\ 1\ 0)_\beta$ peak position. Generally, the data for 10 and 25 % Zr is more scattered than for the 5 % Zr composition, which makes it more difficult to unveil possible correlations.

4.3 Changes upon Annealing

This section will discuss annealing-induced changes in hardness, ΔH, and diffraction profile, mainly focusing on the $(1\ 1\ 0)_\beta$ peak. First, results on the 5 % Zr sample will be elaborated, representatively. Afterwards, all compositions will be considered, though results are similar. Then, the anneal hardening kinetics will be analyzed.

4.3.1 5 % Zr Samples

Figure 4.10 summarizes the results of annealing at 300, 350 and 400 °C. The annealing times were 15, 30, ..., 90 min, and 2 and 4 h. This temperature range is considered first, because it has 8 annealing times, in contrast to 2 at higher and lower annealing temperatures.

Intermediate Temperature: Hardening

Clearly, annealing has a considerable effect on the hardness. Even the shortest treatment, 15 min, at 300 °C caused a hardness increase of 50 HV0.5. At 400 °C,

the initial increase was even stronger, measuring 74 HV0.5. At 30 min, the hardness increase of the 300 °C sample reaches 73 HV0.5, and remains at this value up to 75 min. Eventually, at 2 and 4 h, its hardness stabilizes at 80 HV0.5 higher than the as-HPT specimen. The 350 °C hardness, in contrast, almost continuously increases with the exception of the value at 75 min. It is unclear whether this value is an outlier or not. At 350 °C and 4 h, the annealing-induced hardening reaches a maximum, 100 HV0.5. At 400 °C, the increase peaks at a value of 85.8 HV0.5 after 75 min, and subsequently drops down again, and overlaps with the 300 °C measurements at 2 and 4 h.

Intermediate Temperature: Peak Broadening

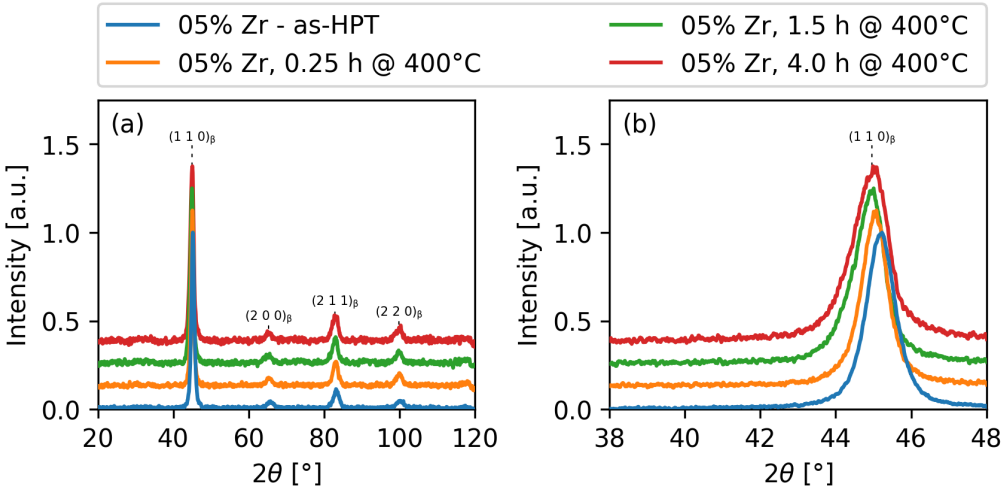

FIGURE 4.11: X-Ray diffractogram of an 5 % Zr as-HPT sample and its $^1/_8$th sections, that have been annealed at 400 °C during 15 min, 90 min and 4 h, with suffixes 15m, 90m and 4 h, respectively: large 2θ-range diffractogram (a) and cropped $(1\ 1\ 0)_\beta$ peak (b).

The $(1\ 1\ 0)_\beta$ peak width, in the central graph of Figure 4.10, decreases by annealing for 15 min to about 0.82°, seemingly independent of annealing temperature. Even more, the initial decrease also seems independent of as-HPT FWHM, because this value was higher for the 350 °C and 400 °C samples than for the 300 °C sample, at 0.94, 0.92 and 0.87°, respectively. Further investigation is however required to verify whether this is the case if the as-HPT samples all have similar $(1\ 1\ 0)_\beta$ FWHM.

To investigate the strong increase in FWHM during annealing at 400 °C, Figure 4.11 displays both the entire diffractogram (a), and the $(1\ 1\ 0)_\beta$ peak (b) for samples annealed at 15 min, 90 min and 4 h. Compared to the as-HPT state, no new peaks emerge, though they might be obscured by the high amplitude of background noise signal, which may partially be caused by the small sample size of the $^1/_8$th sections. The cropped $(1\ 1\ 0)_\beta$ peak graph, however, clearly shows the increasing FWHM,

which can easily be seen as a lower slope of the peak shape. In all cases, the peak shape seems to remain symmetric, but there is a slight shift to lower 2θ-values for intermediate annealing times, which is visible in Figure 4.10 as well. The peaks at higher hkl-values, however, seem to become slightly more asymmetric.

Intermediate Temperature: Peak Position

For all presented annealing temperatures, FWHM generally seems to increase with increasing annealing time. The lowest annealing temperature, 300 °C, causes a slight increase in peak width with increasing annealing time, from 5° at 15 min to 0.83° at 4 h. Second, the trend at 350 °C seems to increase with time as well, even though the FWHM at 90 min, 0.81°, is slightly lower than the initial value, 0.83°. At 4 h, the width increases to 5°, which is still lower than the as-HPT value of 0.94°. Finally, at 400 °C, the FWHM monotonically increases from 0.83° at 15 min, to 0.97 and 1.13° at 90 min and 4 h, respectively.

The annealing process does not significantly impact the $(1\ 1\ 0)_\beta$ peak position, as can be seen in the rightmost graph of Figure 4.10. Similar to the observations from as-cast to as-HPT state, the changes in $(1\ 1\ 0)_\beta$ peak center due to the annealing process are in the same order of magnitude as the spread on the as-HPT samples. Even in the isothermal sets, there is no clear trend: none of the three presented temperature series increase or decrease monotonically.

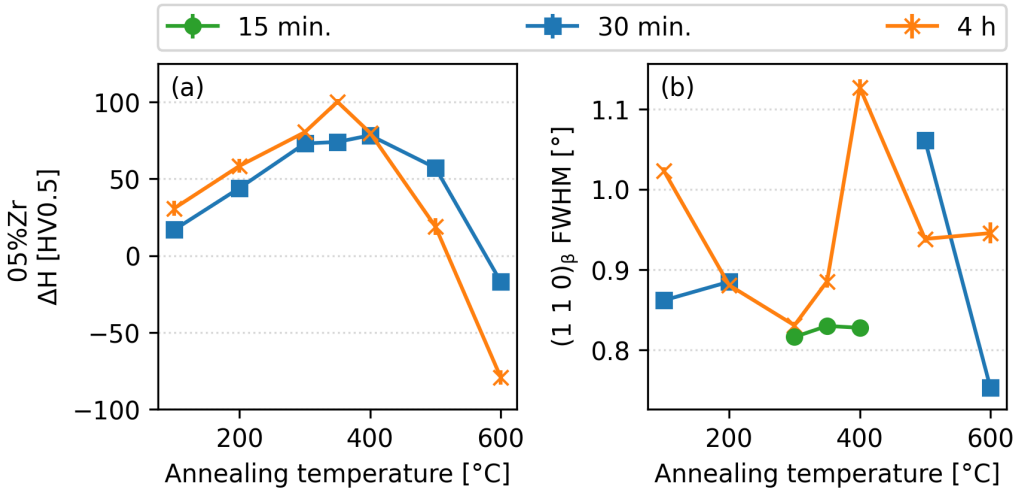

Figure 4.12: Hardness change -ΔH- (a), and $(1\ 1\ 0)_\beta$ peak FWHM (b) in function of annealing time, for short and long annealing time.

The influence of annealing temperature was researched further by annealing at 100, 200, 500 and 600 °C as well, for 30 min and 4 h. These results are combined with the results of the discussion above into Figure 4.12. Unfortunately, the FWHM at 30 min was not available for annealing temperatures 300, 350 and 400 °C, so the

value at 15 min was used instead. Data on the $(1\ 1\ 0)_\beta$ peak center position was not included, as no significant changes were observed.

Complete Temperature Range: Hardening

Considering the hardness change first, two trends become evident. First, the curves for both short and long annealing time have the same distinct shape. In both cases, annealing causes a hardness increase up to 350-400 °C. Then, the effect weakens at 500 °C, and annealing at 600 °C causes softening compared to the as-HPT state. Second, longer annealing time enhances the hardening effect up to 350 °C. Similarly, at temperatures above 400 °C, a longer annealing time results in a stronger hardness decrease with respect to the 30 min cases.

Complete Temperature Range: Peak Broadening

In terms of peak width, the trends are more complex, as can be seen in Figure 4.12 (b). Observing both the 15 and 30 min datapoints, the curve seems slightly M-shaped. In this case, the mechanism responsible for the initial peak narrowing observed earlier, is strongest at intermediate temperature, while the peak width is more similar to the original value (0.91°) at 100 and 200 °C. At 500 °C and 30 min, the peak width increases from 0.91° in the as-HPT state to 1.06°, while it decreases to 0.75° in the case of 600 °C.

Annealing for 4 h, in contrast, results into a rather W-shaped curve. It is remarkable that, at 100 °C and 4 h, the peak width is near to the maximal observed value. Upon inspection of the diffractogram (not shown here), multiple peaks related to oxides, such as Nb_2O_5, were observed. Hence, the oxide layer was not sufficiently removed before XRD, which may cause the broadening. At 200 and 300 °C, longer annealing time does not result in any additional broadening. The peak width reaches a maximal value at 400 °C, and remains at a lower, constant level for 500 °C and 600 °C.

Analysis of Hardening Kinetics

The hardness data presented in Figure 4.12 (a) allows to perform an analysis of the hardening kinetics, following the method of Rupert et al. [61], as explained in section 3.6.
Now, Figure 4.13 shows the results of this analysis, using the same data on hardness change as Figure 4.12 (a). To enhance readability, the temperature values in °C were added at the top of the graph. The errorbars indicate the pooled standard deviation $s_{\Delta H}$ on the hardness change, as explained in section 3.9. The asymmetry of the errorbars of the 100 °C sample is caused by the logarithmic function. Overall, the curve fits the data well, with an R^2 value close to 95%. As indicated in the bottom-left corner of the figure, the activation energy of the mechanism responsible for anneal hardening is 92 ± 1.0 meV.

To summarize, this section discussed the anneal hardening phenomenon in the 5 % Zr sample. Annealing at 350 °C caused the largest hardness increase compared to

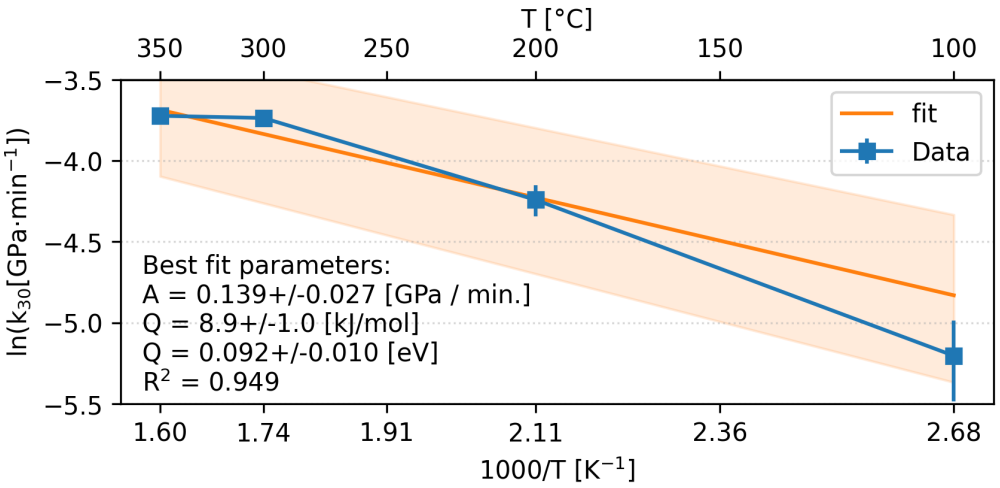

Figure 4.13: Arrhenius plot of hardening constants after 30 min of annealing for 5 % Zr samples.

the as-HPT state. Lower temperature annealing leads to a limited hardness increase. At temperatures of 400 °C and above, increasing annealing time causes decreasing hardness after a strong initial anneal hardening. Furthermore, at 600 °C and 30 min, the observed hardness was already lower than the as-HPT state. In terms of $(1\ 1\ 0)_\beta$ FWHM, short annealing times lead to decreased peak width, with the only exception of 500 °C. For longer annealing time, at low and intermediate temperatures, there is no significant broadening. At 400 °C, maximal peak width is reached, and the width at 500 and 600 °C is slightly higher than the as-HPT state.

4.3.2 Annealing Changes with Respect to Composition

The following paragraphs present the same results as above, including the 10 and 25 % Zr compositions.

A complete overview of changes in hardness change, ΔH, $(1\ 1\ 0)_\beta$ FWHM and center position induced by annealing is displayed in Figure 4.14. The upper row presents the values of 5 % Zr, discussed above.

Intermediate Temperature: Hardening

First, we consider the hardness change, in the leftmost column (a, d, g). As can be seen, at any annealing temperature, the hardness increased compared to the as-HPT state. The initial hardening behaviour at intermediate temperatures in the 10 % Zr samples is similar to the 5 % Zr sample, with an increase of about 60-80 HV0.5. The initial hardening in the 25 % Zr sample, in contrast, is more complex. At 400 °C, the initial increase barely surpasses 40 HV0.5, while it exceeds 80 HV0.5 at 350 °C.

The 10 % Zr sample is the only sample with a detailed, low-temperature hardening series, at 150 °C. There, the linear hardening slope is clearly visible. The hardness

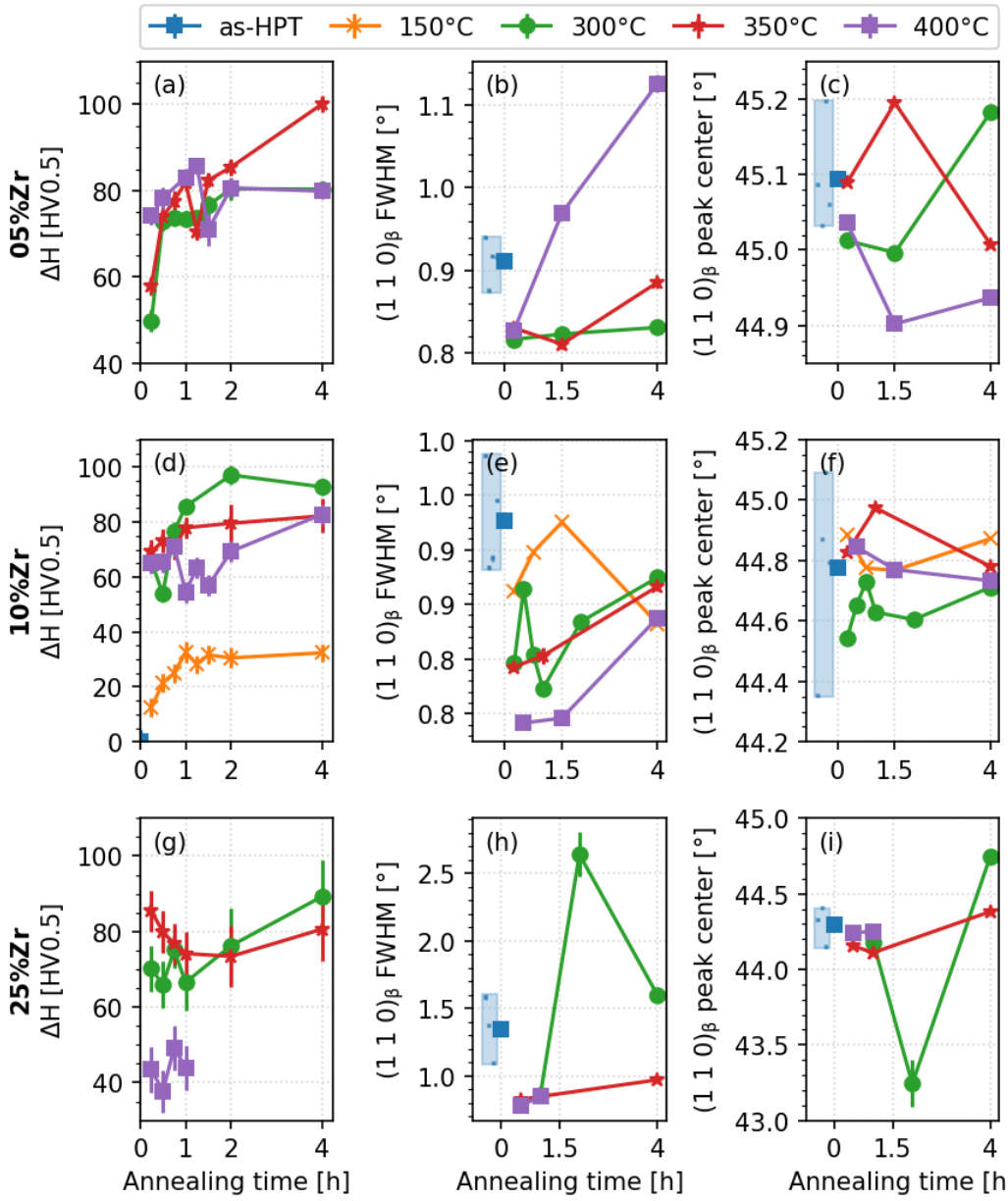

FIGURE 4.14: Overview plot showing hardness change (a, d, g) and $(1\ 1\ 0)_\beta$ peak FWHM (b, e, h) and center position (c, f, i) for all three compositions, as rows (5 % Zr: a-c, 10 % Zr: d-f, 25 % Zr: g-i).

increases at a rate of about 32.5 HV0.5 $\cdot$ min^{-1}, reaching a maximal value after about 1 h. Longer annealing time does not cause any hardness increase. This behaviour is very similar to the reported anneal hardening behaviour in nanocrystalline Ni-W alloys, as reported by Rupert et al. [61].

The other annealing temperatures -300 °C to 400 °C- do not exhibit linear hardening behavior. Focusing on the 10 % Zr sample first, the hardness of the 300 °C time-series drops slightly at 30 min, and increases to an overall hardness maximum at 2 h, after which it again dips slightly. The drop at 30 min may be caused by the following: two different as-HPT disks were used to compose the 300 °C hardening curve. There, the 15 and 45 min samples originated from a different disk than the 30 min sample. Due to time constraints, it was not possible to perform the experiments again using yet another as-HPT disk, which may have resulted in a different curve. The 350 °C sample gradually hardens after the strong initial hardness increase up to 1 h. Afterwards, its hardness seems to remain constant, though this is difficult to assert with certainty, due to the large standard deviation on the measurements at 2 and 4 h. The 400 °C curve has a W-shape, with a slight hardness decrease after initial hardening. The hardness recovers from this decrease at 2 and 4 h annealing times, and the final hardness is similar to the 350 °C sample.

In the 25 % Zr sample, the 300 °C sample does not seem to significantly harden after the initial hardness increase in the first hour of annealing. Afterwards, however, it reaches a maximal value at 4 h, though the error bars are high for annealing time exceeding 1 h, which is also the case in the 350 °C sample. This high error seems to be caused by the original as-HPT disk, since the 2 and 4 h samples for 300 °C and 350 °C originate from the same as-HPT disk. Indeed, the standard deviation on the as-HPT and annealed samples varies between 8-10 HV0.5. These samples have the highest standard deviation of all samples included into the presented dataset. The 350 °C exhibits decreasing hardness up to 1 h, after which it roughly remains constant. At 400 °C, only measurements up to 1 h were made. There, no obvious trend is present, the annealing-induced hardness change seems to remain at a constant level.

Intermediate Temperature: Peak Broadening

In terms of $(1\ 1\ 0)_\beta$ FWHM, the trends seem similar to the 5 % Zr case. For all studied annealing temperatures, in all compositions, there was an initial decrease in peak width. Afterwards, the peak broadens with increasing annealing time. Again, in the 10 % Zr case, the 300 °C curve seems to fluctuate at low annealing time, which may be caused by the 15 and 45 min samples originating from a different HPT sample. Also, the 10 % Zr 300 °C and 350 °C FWHM curves overlap at long annealing times. The 10 % Zr 400 °C behaves similarly, but its peak width is lower compared to the 300 °C and 350 °C samples. The 150 °C sample always has a higher peak width, though the peak width decreases at 4 h of annealing. Remarkably, the peak width of the as-HPT sample that was used for the 10 % Zr had a FWHM of 0.89°, which is lower than most as-HPT peak widths. Unfortunately, the FWHM was not measured for all as-HPT samples, so it remains difficult to quantify the temperature effect on change in FWHM.

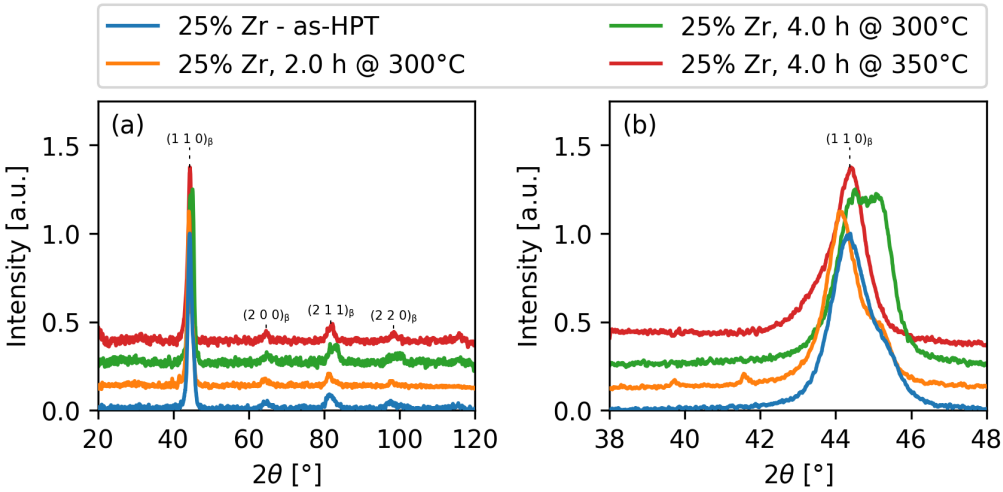

FIGURE 4.15: X-Ray diffractogram of as-HPT 25 % Zr sample and annealed at 300 °C for 2 and 4 h, and 350 °C for 4 h samples: large 2θ-range diffractogram (a) and cropped $(1\ 1\ 0)_\beta$ peak (b).

In the 25 % Zr case, the FWHM after annealing 30 min seems to be independent of temperature or as-HPT FWHM. In addition, at 1 h, the FWHM overlaps as well, at 0.85°. Then, the 350 °C sample's FWHM increases slightly at 4 h. The 300 °C sample annealed for 2 h, however, has a peak width of 2.64°, which is almost double the maximal recorded FWHM value in the other two compositions. So, Figure 4.15 (b) shows a diffractogram cropped to the $(1\ 1\ 0)_\beta$ peak. There, the origin of the high FWHM of the 300 °C 2 h sample can immediately be seen. The peak shape seems to be composed of two distinct peaks, a tall one at the left-hand side, and a lower peak at the right-hand slope. These peaks are overlapping just enough to still be able to interpreted as a single peak by the fitting algorithm. In the 300 °C 4 h sample, the height of both peaks seems to be equal. Inspecting the large 2θ-range diffractogram (Figure 4.15 (a)), the measurement noise is so high that it is unclear whether new diffraction peaks emerged. These observations are also reflected in the movement of the $(1\ 1\ 0)_\beta$ peak center positions, on the rightmost graph of Figure 4.14.

Intermediate Temperature: Peak Center

With exception of the 25 % Zr 300 °C 2 h peak shift, the $(1\ 1\ 0)_\beta$ peak center position does not seem to vary much with different annealing time or composition, as was already the case for the 5 % Zr samples.

Complete Temperature Range: Hardening

Figure 4.16 now includes the hardness (a) and $(1\ 1\ 0)_\beta$ peak width (b) for varying annealing times with respect to temperatures. Considering the hardness curves first, Figure 4.16 (a), there is a strong similarity between compositions. For annealing

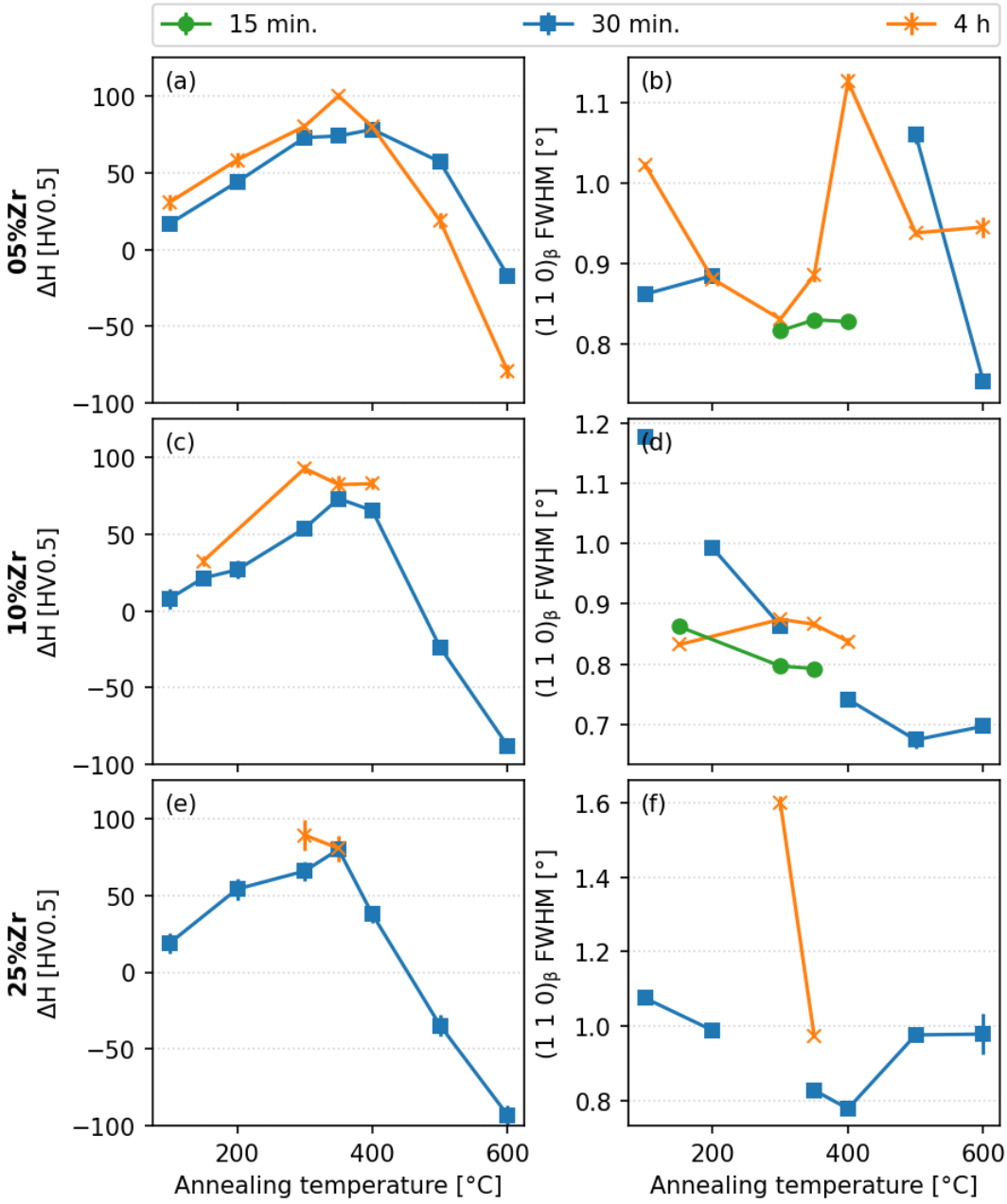

Figure 4.16: Overview plot showing hardness change (a, c, e) and $(1\ 1\ 0)_\beta$ peak FWHM (b, d, f), as columns, for all three compositions, as rows (5 % Zr: a-b, 10 % Zr: c-d, 25 % Zr: e-f).

temperatures up to 350 °C, increased annealing temperature causes a stronger initial anneal hardening. Similarly, in the same temperature range, annealing for 4 h results in an even higher hardness increase, though the difference between the 30 min and 4 h hardness change is rather low.

Increasing annealing temperature above 350 °C does not yield higher anneal hardening. Moreover, in both 10 and 25 % Zr cases, annealing at a temperature of 500 °C or higher caused a hardness decrease compared to the as-HPT state. No 4 h annealing time experiments were performed at high ($\geq$ 500 °C) or low temperatures ($\leq$ 200 °C), for the 10 and 25 % Zr compositions, so nothing can be inferred about the annealing time effect at these temperatures.

TABLE 4.1: Maximal annealing-induced hardening for each composition.

Alloy	Absolute Hardness [HV0.5]	ΔH [HV0.5]	ΔH [%]	Annealing Time [h]	Annealing Temperature [°C]
5 % Zr	430	100	30	4	350
10 % Zr	436	97.2	28.6	2	300
25 % Zr	449	89.3	25.0	4	300

Overall, the maximal hardness change achieved by anneal hardening is presented in Table 4.1. The highest absolute hardness could be reached in the 25 % Zr sample, even though the relative hardening by annealing, compared to as-HPT hardness, was highest in the 5 % Zr sample.

Complete Temperature Range: Peak Broadening

In terms of $(1\ 1\ 0)_\beta$ FWHM, the most remarkable observations on Figure 4.16 (b) have already been described above. In the 25 % Zr case, annealing after 30 min roughly results in the same peak width at all temperatures. Interesting is the 100 °C 30 min case for the 10 % Zr composition, there the FWHM is rather high. It is, however, unknown what the FWHM of this exact sample in as-HPT state was. Possibly, it was quite large, because figure 4.14 suggests that, especially for the 10% composition, the FWHM of as-HPT disk may be quite large.

Correlation Between Hardness and FWHM

To better grasp whether there is any correlation between the hardness change, composition, and FWHM, Figure 4.17 summarizes those values.

As can be seen, most data points are grouped together in the top left corner. On the $\Delta H = 0$-line, the as-HPT samples are visible. On that line, the FWHM of the 25 % Zr samples is higher than those of the 5 and 10 % Zr samples, which is probably due to the worse mixing in those samples, as observed earlier. Most

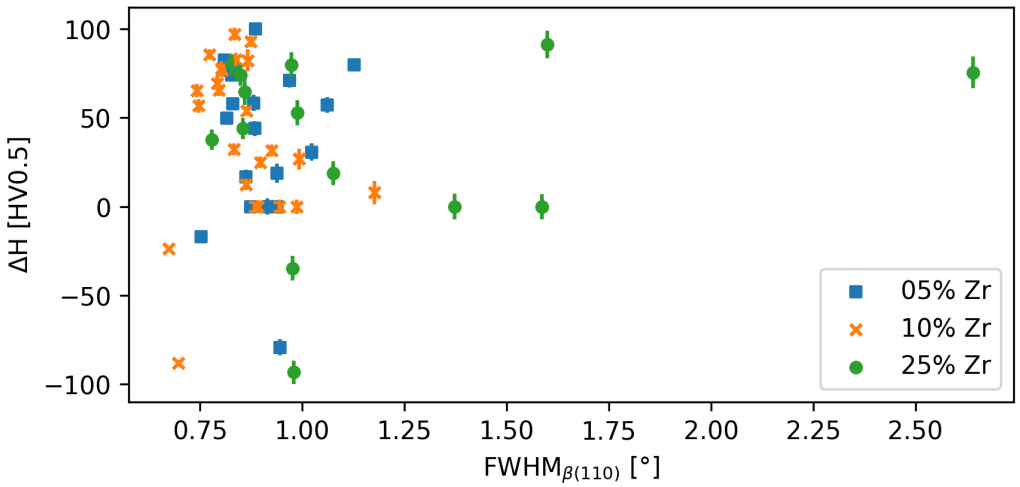

Figure 4.17: Annealing-induced hardness change vs. FWHM for all samples where both values were recorded.

datapoints with positive hardness change are then grouped together to the top left of the as-HPT samples. Such behaviour is expected as the defect density decreases due to annealing, causing better-defined peaks [66]. The same effect causes the anneal hardening phenomenon.

Considering the samples with negative hardness change next, they are, in most cases, shifted to the bottom left side of their former, as-HPT counterpart. These observations also align with the expected results. It has been established that the hardness decrease is caused by grain growth, while the decrease in defect density also takes place. Both processes decrease peak width, which is reflected by the fact that these points have the lowest overall $(1\ 1\ 0)_\beta$ FWHM.

Finally, some of the 25 % Zr samples have a significantly higher FWHM. As discussed earlier, it is unclear what caused the split peaks in the diffractogram. These measurements should be performed again using chemically homogeneous as-cast samples to verify whether the observations are repeatable or stem from insufficient mixing.

4.3.3 Anneal Hardening: Composition and Temperature Dependence

In the following the influence of temperature and composition on the hardness increase by annealing is compared. For this purpose, Figure 4.18 displays the annealing-induced hardness change after 30 min (a) and 1 h (b) respectively. These results show multiple remarkable trends.

First, considering 30 min, the anneal hardening peaks at 350 °C, for the 10 and 25% compositions. Furthermore, the hardness increase at this temperature seems roughly the same in all studied compositions. Second, leading up to 350 °C, the slope

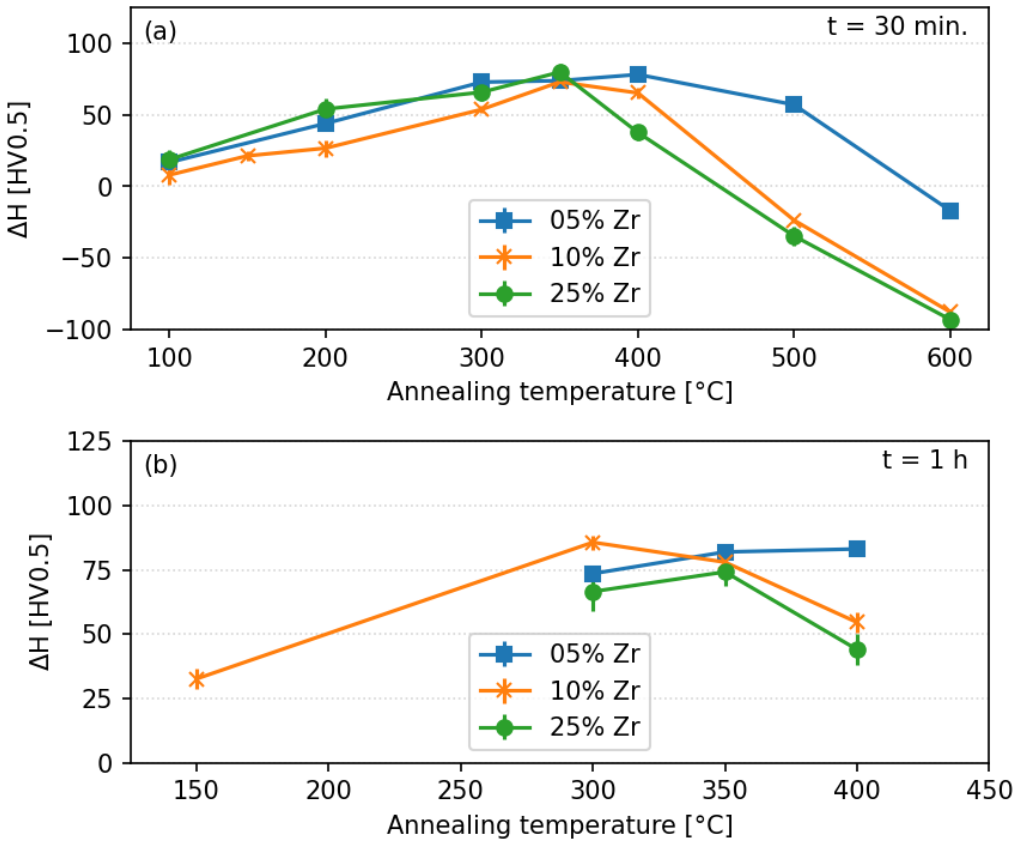

FIGURE 4.18: Annealing-induced hardening after 30 min (a) and 1 h (b) for all studied samples and temperatures.

of all 30 min curves seems similar. In addition, at all temperatures up to 350 °C, the curves of the 5 and 25 % Zr almost overlap. However, at 400 °C and above, the overall hardening declines most strongly for the 25 % Zr curve, while the 5 % Zr samples seem less affected.

After 1 h, however, several differences are visible. First, the overall hardness already declines above 300 °C for the 10 % Zr sample and above 350 °C for the 25 % Zr sample. Just like at 30 min, the 5 % Zr sample is still unaffected.

Analysis of Hardening Kinetics

The analysis of hardening kinetics was performed analogue to the 5 % Zr case presented above, and Figure 4.19 visualizes the results. In all cases, the hardness change after 30 min was used to calculate the kinetic parameter k. The Arrhenius equation fits the results well: the minimum of the R^2-value is 94.6%. The estimated coefficient A and apparent activation energy Q, consider the standard deviation on $s_{\Delta H}$, while the R^2 only reflects how well the mean values fit the Arrhenius equation.

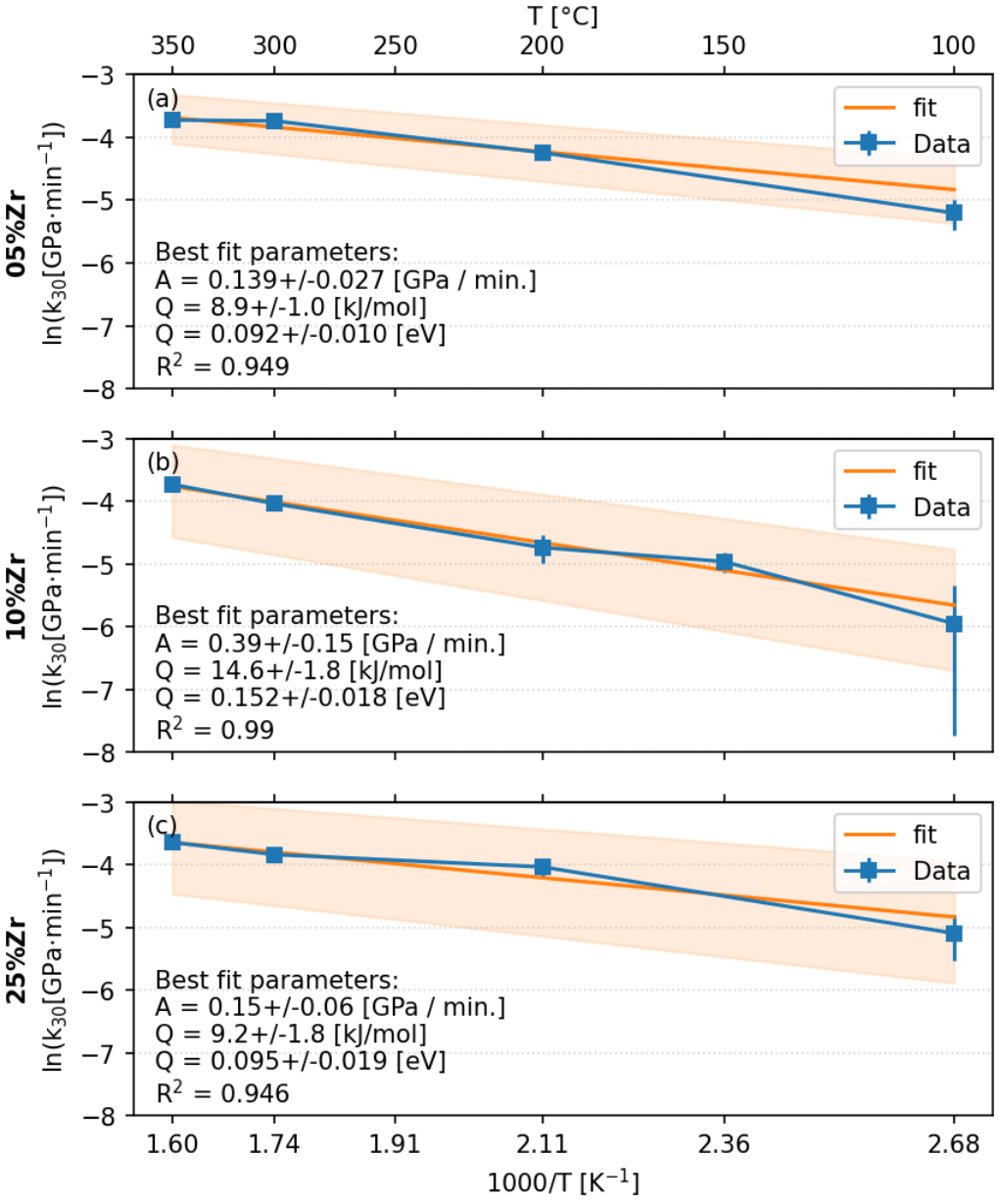

Figure 4.19: Overview plot showing the fit of Arrhenius equation on 30-minute hardening kinetic constant for 5 % Zr (a), 10 % Zr (b) and 25 % Zr (c).

Hence, the uncertainty on the parameters of the 10% parameter are the largest of all presented, while its R^2-value is considerably better.

The previously observed overlap between the 5 and 25 % Zr samples is well-reflected in the fitting results. Both the pre-exponential coefficient and apparent activation energy fall within the same range.

The 10 % Zr sample, on the other hand, has slightly higher values for both parameters. The link with hardness values can be easily explained. As can be seen on Figure 4.18, the annealing-induced hardening for that composition is lower than for 5 and 25 % Zr. Then, the hardening rate, is lower as well, as it is equal to the hardness value divided by 30 min, meaning the slope on the logarithmic plot will be lower as well. Since the slope is proportional to -Q, the absolute value of the activation energy is larger. Conversely, from a theoretical standpoint, this observation can also be explained: if the energy barrier for thermal activation of the hardening process is higher, this barrier will be overcome less frequently, meaning the observed hardening is lower. The pre-exponential constant is equal to A = exp(intercept, i.e. $\frac{1}{T} = 0$), which also decreases for curves that lie lower on these plots. The physical interpretation, however, of this parameter is less intuitive, as the intercept would be at infinitely large temperature.

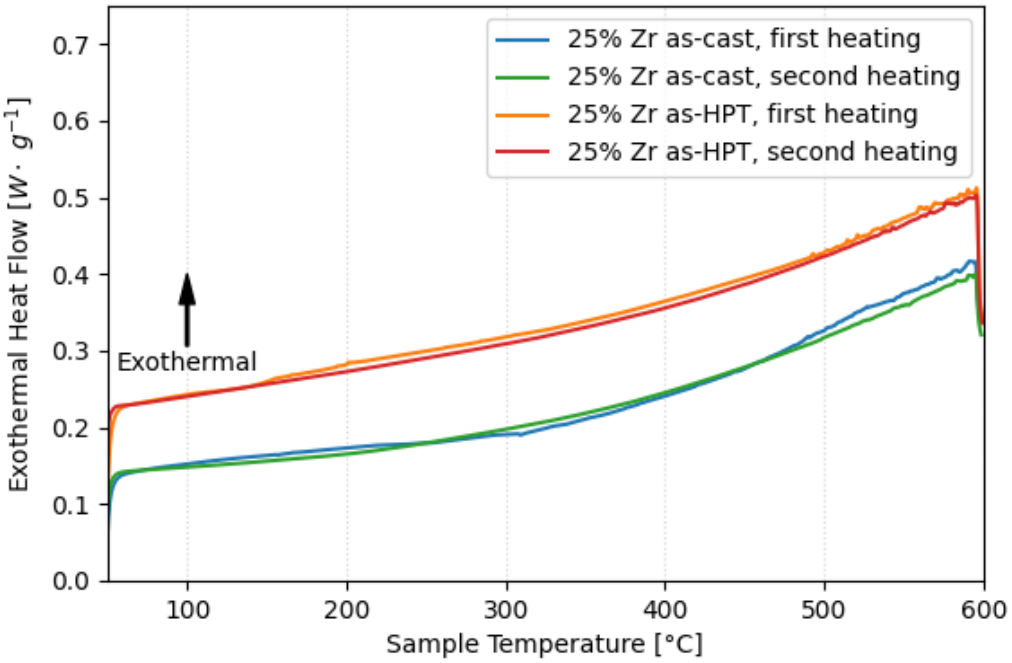

FIGURE 4.20: DSC curve of as-cast and as-HPT 25 % Zr sample. Note that all curves are offset in y-direction, for readability. Hence, the labels on the y-axis should be used as a scale, rather than absolute heat flow values.

4.4 DSC

Figure 4.20 displays the DSC curves of as-cast and as-HPT 25 % Zr samples. In both cases, up to around 250 °C, the curves corresponding to the first heating cycle display larger exothermal heat flow than those of the second heating cycle. In the as-HPT sample, this exothermal continues up to the maximal temperature value.

In both samples, the effect of oxidation can explain the exothermic difference between first and second heating cycles. After the measurements, both samples were oxidized, supporting this theory. In addition, defect annihilation and grain growth in the as-HPT is expected, though no distinct peaks are observed. The results of Gubicza et al. on HPT-processed Ni-1.3wt.%(Mo, Al, Fe), indicate that the height of DSC peaks are below 0.01 $W \cdot g^{-1}$ for defect annihilation and around 0.03 $W \cdot g^{-1}$ for grain growth, using a heating rate of 40 $K \cdot min^{-1}$ [22, 23].

Considering the low DSC peak height of those processes, it is possible that the oxidation of our samples eclipses these small peaks. In addition, the lower heating rate used here could cause the peaks to be broadened over the x-axis, so that they are not detectable in our case. Hence, a higher heating rate and more protective atmosphere might yield more useful results.

4.5 Transmission Electron Microscopy

Figure 4.21 compares as-HPT and annealed states of 5 % Zr samples. As can be seen in all images, HPT has caused strong grain size refinement. In all cases, the grain size seems to lie between about 50 and 100 nm, meaning the annealing treatment did not cause significant grain growth.

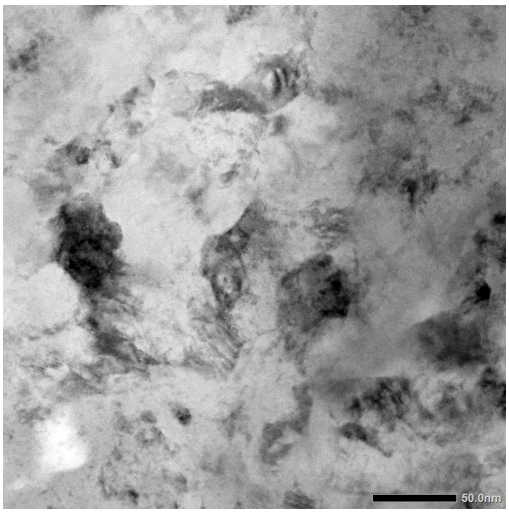

(A) As-HPT.

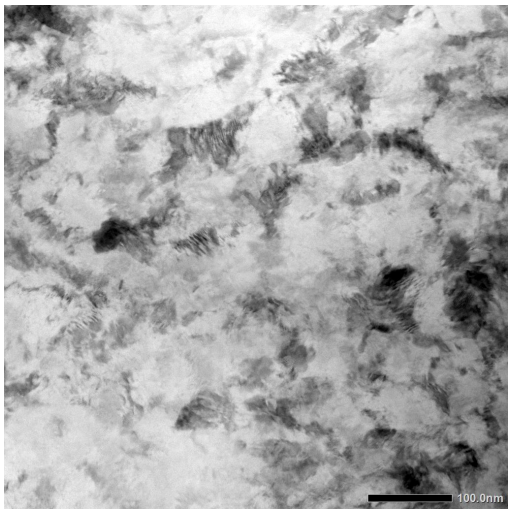

(B) 400 °C for 15 min

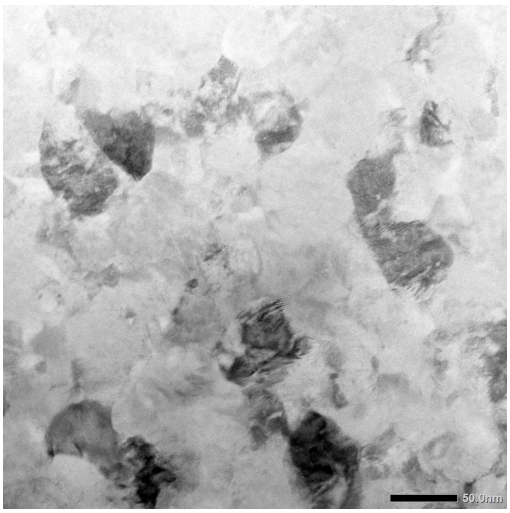

(C) 400 °C for 4 h.

FIGURE 4.21: Representative transmission electron micrographs of 5 % Zr samples. Note that the scale bar length is 100 nm in Figure 4.21b, and 50 nm for the other 2 images.

Chapter 5

Discussion

5.1 Composition fluctuations

As explained in section 4.1, both as-cast ingots and as-HPT samples have compositional inhomogeneities. The cause of these inhomogeneities was further investigated in this work, but the following subsubsection highlight some findings from literature that can help determine the cause.

First, both in binary and ternary β-stabilized Ti alloys, dendritic solidification has been observed. Examples are Ti-Nb [5], Ti-Ta [75], Ti-Nb-Zr medium-entropy

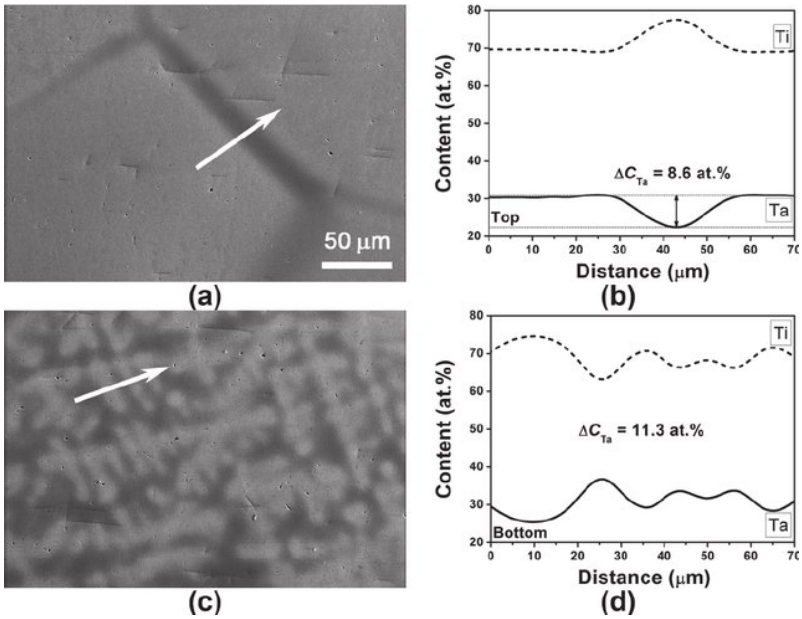

FIGURE 5.1: As-cast Ti-30Ta ingot with 10 remelting cycles. (a) and (b): Top of ingot. (c) and (d): Bottom of ingot. (a) and (c): BSE micrographs, EDX line scan positions indicated by white arrows. (b) and (d): corresponding EDX line scans. Copied from Zhang et al. [75].

Table 5.1: Processes activated at different stages during sample processing and their effect on grain size and $(1\ 1\ 0)_\beta$ FWHM.

Stage	Process	Effect on	
		Grain Size	$(1\ 1\ 0)_\beta$ FWHM
HPT	Grain Fragmentation	↓	↑↑
	Grain Boundary Migration	=	↓
Anneal	Anneal Hardening	=	↓
	Grain Growth	↑	↓
	Precipitation	N.A.	↑

alloy [29], Ti-Nb-Zr (same composition as 5 % Zr composition in this work) [37]. As Figure 5.1 shows, solidification causes rejection of dissolved tantalum. Still, the magnitude of composition variation is lower than the EDX results presented in this work, where fully zirconium-depleted regions were observed (Fig. 4.1a). Indeed, the study by Hu et al. on Ti-Nb-Zr medium-entropy alloys suggest that the partition coefficient is the lowest for zirconium [29]. Both of these findings suggest that, in addition to solute rejection by dendritic solidification, insufficient mixing during arc-melting are possible causes for the compositional variations in this work. To promote mixing during arc-melting, a finer feedstock should be used and, if necessary, the ingot should be remelted more times. To dissolve dendrites, multiple authors have succesfully used a recrystallization heat treatment by heating the sample to 1000 °C during 24 h [5, 37], while K. Bartha obtained quite homogeneous samples using only 810 °C for 4 h [4].

Chemical fluctuation effect on hardness

The chemical inhomogeneity may affect the hardness of as-HPT and annealed samples in two ways. First, solid solution may cause additional hardening in as-cast, as-HPT and annealed samples. Considering the slightly higher maximal hardness values of the 25 % Zr as-cast samples compared to 10 % Zr, in Figures 4.2b and 4.2a, respectively, suggests that solid solution hardening occurs in the coarse-grained samples. Second, for as-HPT and annealed samples, increasing alloying content may also decrease saturation grain size, enhancing hardness [35, 56, 16]. In summary, local fluctuations in Zr-content may cause fluctuations in measured hardness as well. This conclusion is experimentally supported by the results in Figure 4.3. In that graph, the length of the errorbars (i.e. standard deviation) of zirconium content scales well with the standard deviation on Vickers hardness.

5.2 Microstructural changes and their effect on hardness

The two distinct processing stages used in this work, HPT and subsequent annealing, strongly modify the material structure and, consequently, properties. Table 5.1

summarizes these processes and their general effect on grain size and $(1\ 1\ 0)_\beta$ FWHM. The text below details how the results presented above indicate the occurence of these processes.

As briefly explained in the literature study, high-pressure torsion strongly reduces the grain size, which causes a sharp increase in $(1\ 1\ 0)_\beta$ FWHM. The introduced defects also contribute to peak broadening. The grain size eventually saturates as fragmentation processes are balance with grain boundary migration.

During annealing, at least three major processes are active. First, the anneal hardening process, consisting of defect annihilation in both grain interior and grain boundary, which has been observed in multiple similar studies. Second, above a certain temperature threshold, grain growth will occur. Finally, the present observations indicate a third mechanism is active, which might be precipitation, based on similar studies on β-Ti alloys.

5.2.1 HPT

Grain Size Refinement

A strong grain size refinement has taken place by HPT, as can be seen from the TEM micrographs, see Figure 4.21. The significant strengthening by HPT, in all compositions, up to a 35 % hardness increase, further evidences the grain size refinement. Consequently, as expected, the decreasing grain size is reflected in the $(1\ 1\ 0)_\beta$ FWHM as well, causing a significant broadening, see Figure 4.9.

The $(1\ 1\ 0)_\beta$ broadening is rather strong, despite the fact that compositional inhomogeneities may already cause peak broadening in the as-cast samples to some extent: Complete demixing of Zr-rich and Zr-lean phases in the 25 % Zr composition resulted in two seperate XRD peaks, where each peak corresponds to a phase that is well-mixed, as can be seen in Figure 4.1a. Hence, in a case where the entire ingot was as perfectly homogeneous single phase β, its FWHM might be comparable. If this reasoning is valid, then HPT would cause a peak broadening from 0.25° to over 1.25°, as measured by FWHM.

Methods such as Warren-Averbach and Williamson-Hall allow to estimate both grain size and internal stresses by measuring the width of multiple diffraction peaks [66]. Here, these methods could not be applied successfully for a number of reasons. First, there were no well-resolvable higher order reflections of a certain lattice family, excluding the Warren-Averbach method. Second, most peaks, except for the $(1\ 1\ 0)_\beta$ peak, had low intensity, high noise and extensive broadening, meaning the FWHM could not be measured accurately. In addition, the instrumental broadening has not been established. Specifically, the calculated strain often was larger than 3 %, while the intercept was negative, meaning a negative grain size, both are unrealistic results. Still, the extensive broadening clearly indicates a small grain size and possibly also high defect density, both resulting from the grain fragmentation process.

Grain Boundary Migration

Based on literature, the grain size saturation regime should be reached well before 50 turns, see for example source [56]. Based on the uniform hardness distribution in as-HPT samples, as shown in Figure 4.6, it is reasonable to assume that grain size saturation has been reached. Specifically, the absence of a hardness cusp at the radial center of the sample signifies that the applied shear strain at small radial distances is sufficiently high to reach low grain size in the central as well. Similarly, the fact that hardness at low radial distance is equal to that at high radial distance signifies that the restoring mechanism, grain boundary migration, has been active as well. Thus, grain size saturation is reached.

In summary, both the $(1\ 1\ 0)_\beta$ FWHM decrease and hardness increase of as-HPT samples compared to as-cast samples evidence that extensive grain fragmentation took place. Furthermore, the uniform hardness along sample cross-section signifies that the grain size refinement process has saturated and an equilibrium with grain boundary migration, a process restoring grain size, is reached.

5.2.2 Annealing-Induced Hardening

During annealing, three distinct processes may occur, changing the material structure: anneal hardening, grain growth, and a third process which is believed to be precipitation.

Anneal Hardening

First, consider the single-phase anneal hardening. As mentioned above, this process relies on the thermal activation of defect motion, after which they are either annihilate or form a lower energy configuration, either within the grain or at grain boundaries and triple junctions. This process and its effect on hardness can be best observed at low annealing temperatures, as it is then most isolated from the other two processes mentioned above.

Linear Hardening The clearest example of anneal hardening in this study is the 10 % Zr samples that were annealed at 150 °C, as visualized in Figure 5.2. In this case, a clear, linear time dependency can be seen, up to 1 h, with a high R^2-value. Upon longer annealing, no significant hardness changes occur any more. Similar behaviour was reported by Rupert et al. [61], though the relaxation time for their sample was between 300 and 450 min.

All other low-temperature measurements were only carried out at one or two annealing times: 30 min and (sometimes) 4 h. The latter case is presented in Figure 5.3, for 5 % Zr samples. Since, hardness is only recorded at two time values, the relaxation time is not clear. Still, from these two data-points, the hardening seems to confirm the hardening behaviour described above: a strong hardening at low annealing time, and marginal hardening at longer annealing time.

Concerning the linear fit, two interesting observations can be made. First, the intercept is slightly higher than the as-HPT hardness. This is surprising for the

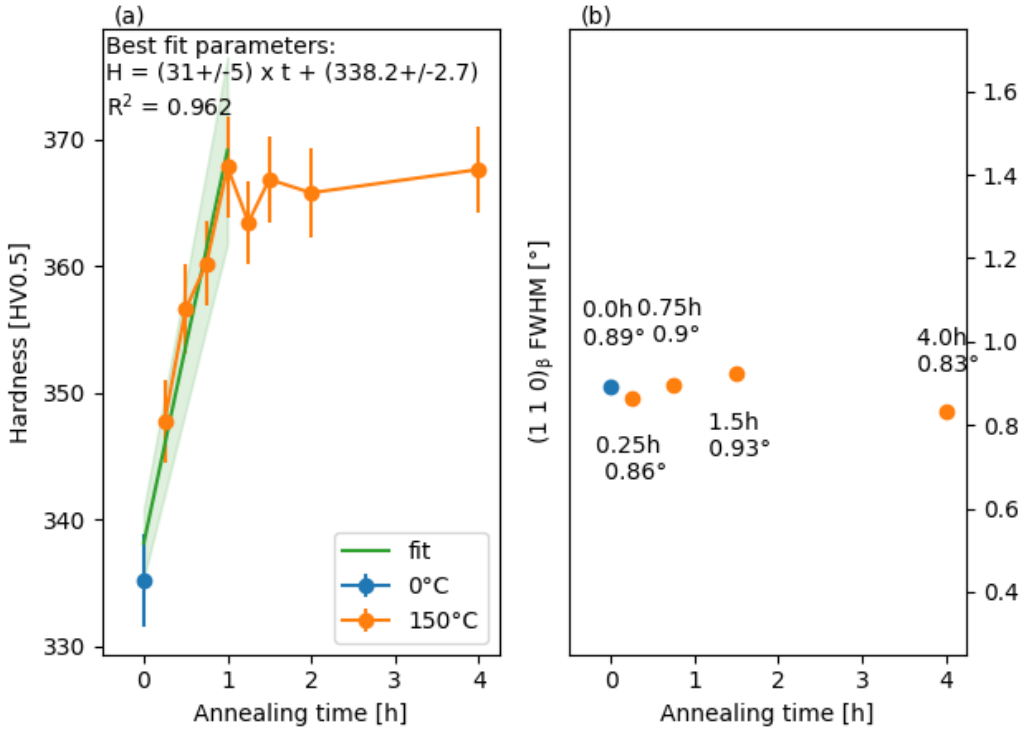

FIGURE 5.2: Anneal hardening in 10 % Zr sample, 0 °C sample refers to as-HPT state, plot shows linear fit from as-HPT state to 1 h.

following reason: if the hardening is fully linear, and its rate scales with temperature following the Arrhenius law, an intercept slightly below the as-HPT hardness would be expected, to account for the time it takes the specimen to heat up in the furnace. Two factors contribute to a slower heat-transfer: first, the furnace was resistance heated and there was no air convection and, second, the sample was wrapped into annealing foil, containing a pouch of trapped air. So, a slightly negative deviation from the linear trend would be expected, rather than the positive one observed here. To more accurately investigate the time-dependency, one requires faster heat transfer, for example by heating the sample through inductive or Joule-heating means. Conversely, a simulation could also indicate whether the required time to heat up the samples might be significant or not. Still, the positive intercept might also be an artifact of the relatively large standard deviation on the hardness measurements compared to the hardness change.

A second observation on the fitted curve is that the shaded area, representing the standard deviation on the fitted parameters, slightly tapers outwards at higher annealing time. In other words, the uncertainty on the fit is increases with annealing time. This tapering is due to the uncertainty on the curve slope, which is multiplied by time.

In summary, a linear trend fits the hardening curve well. The fact that the

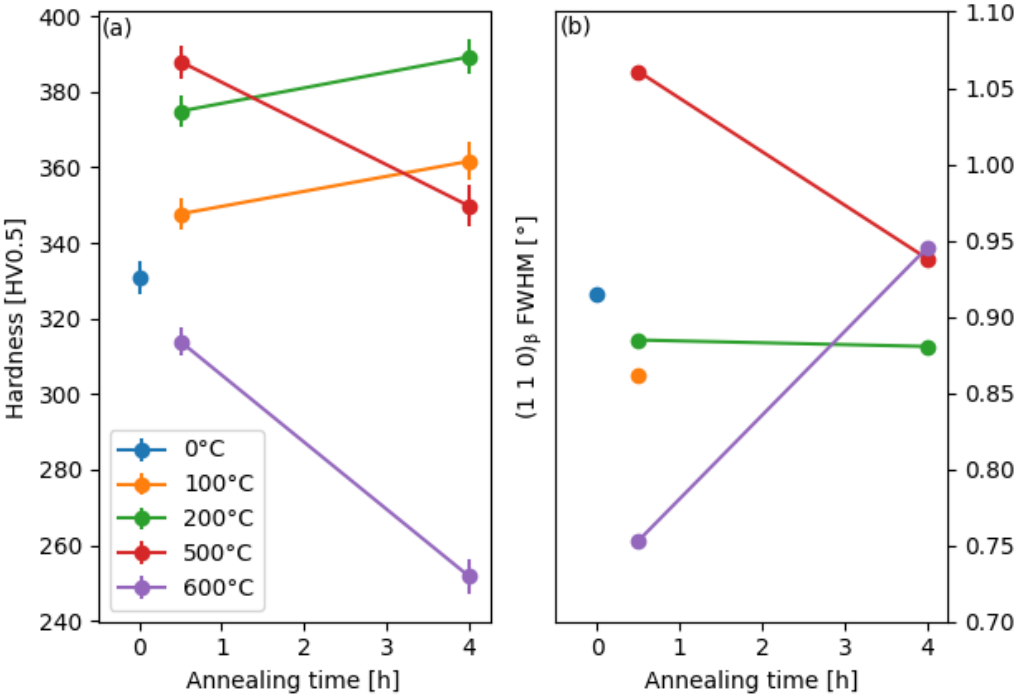

Figure 5.3: Anneal hardening (a) and $(1\ 1\ 0)_\beta$ FWHM (b) in 5 % Zr sample, 0 °C sample refers to as-HPT state.

intercept lies slightly above the as-HPT hardness, may indicate that anneal hardening is a slightly accelerated at very low anneal times, which Latynina et al. have also observed [39].

Anneal Hardening Effect on $(1\ 1\ 0)_\beta$ FWHM In terms of the anneal-hardening effect on the $(1\ 1\ 0)_\beta$ FWHM, the 10 % Zr sample annealed at 150 °C changes only marginally. Figure 5.3 shows the $(1\ 1\ 0)_\beta$ data from some 5 % Zr samples annealed at 100 °C and 200 °C. Note that the 100 °C sample annealed for 4 h was heavily oxidized, so it has been removed from this plot. Additionally, all 7 presented samples originate from the same as-HPT disk. The drop in $(1\ 1\ 0)_\beta$ FWHM after 60 min is stronger for the sample annealed at 100 °C than at 200 °C, though both values are very similar. After 4 h at 200 °C, the FWHM slightly decreases further, compared to the 1 h value, as expected. In summary, anneal hardening causes a slight narrowing of XRD peaks, though the effect is not as pronounced as broadening caused by HPT.

Hardening Mechanism Considering the kinetic values presented in section 4.3, the mechanism responsible for anneal hardening has an apparent activation between 0.09 and 0.15 eV, or 8.9 and 14.6 kJ/mol. Compared to other findings in literature, this range is comparatively low: several publications report values around 50 kJ/mol [61, 39, 22]. Latynina et al., however, report an activation energy of 56 kJ/mol for

commercially pure Al, which decreased to 26.4 kJ/mol upon alloying with 0.393 wt.% Zr. The cause for this decrease is still unknown.

While the values reported by Rupert et al. correspond well to the activation energy for triple-junction diffusion in their alloy system, it is unclear what process corresponds to such low activation energy in the case of this work. First, the activation energy for niobium lattice diffusion in Ti-Nb alloys, reported by D. Moffat [47] lies between 40 and 50 $^{\text{kcal}}/_{\text{mol}} \approx 160$ and 200 $^{\text{kJ}}/_{\text{mol}}$, and these values are similar for Ti and Zr, at 153 and 184 $^{\text{kJ}}/_{\text{mol}}$ for lattice-self diffusion in their respective BCC phases [63]. Second, considering grain boundary diffusion, data on β-Ti alloys is limited, but Chr et al. found that the ratio of the activation energies for grain boundary diffusion vs. bulk diffusion is about 0.68 in coarse grained α-Ti [11]. However, because SPD introduces a high number of defects into the grain boundary, its diffusion activation energy can be considerably lower [66]. Indeed Chuvil'deev et al. found that, based on various experimental results, the grain boundary diffusion activation energy for α-Ti should be around 3-4$k_B T_m$, which is around 0.8 eV, so still higher than the value observed in this work. Third, for triple-junction diffusion, which Rupert et al. suggested to be dominant, no activation energy data could be found. In summary, the responsible mechanisms remains unknown in this work, because lattice and grain boundary diffusion can be ruled out, while no data on triple-junction diffusion is available for β-Ti alloys.

However, a few remarks should be made on the accuracy of the current kinetic analysis. First, the choice to calculate kinetic rates by only considering the hardening after 30 min may not accurately represent the linear hardening regime. As can be seen above (Fig. 5.2), the 10 % Zr sample was still linearly hardening at 150 °C. However, the same cannot be said for the measurements at 300 °C and above, and at 100 and 200 °C, only one measurement was made, after 30 min. As mentioned earlier, Rupert et al. [61] found a saturation time higher than ours at 150 °C, but at 300 °C, this value was lower than 10 min. Hence, annealing at shorter times can provide insight whether the choice for 30 min is justified or not. Second, the used indentation force is quite large, meaning that a large volume of material deforms during indentation. As mentioned in the literature review, see section 2.3, deforming anneal-hardened material re-introduces defects, lowering their hardness [60]. Hence, the actual anneal hardening may be higher than measured here. Both remarks indicate that the hardening rate, especially at higher temperature, might be higher than presented here. Hence, the slope of the Arrhenius-plot would be steeper, meaning the activation energy would be higher, which would reconcile the present low activation energy closer to those reported in literature.

Grain growth

The occurrence of grain growth cannot be denied based on the presented data. Consider for example Figure 4.16. There, for temperatures above 400 °C, the annealing-induced hardness changes declines sharply. In addition, from the 5 % Zr results, this trend continues with extended annealing time. In terms of$(1\ 1\ 0)_\beta$ FWHM, all studied samples at 500 and 600 °C had a decreased peak width compared

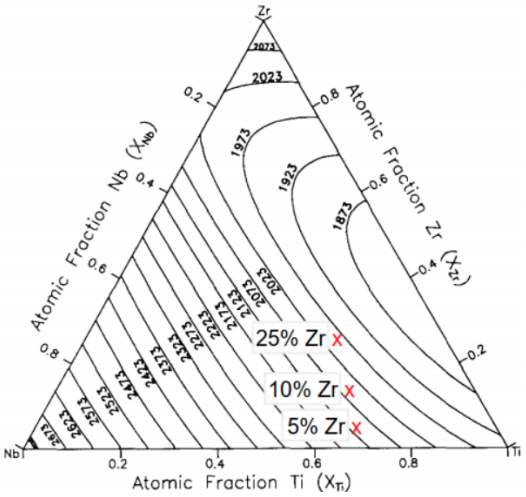

Figure 5.4: Computed liquidus projection [K], copied from Kumar et al [26]. Compositions are indicated on the plot.

to the as-cast state, except for the 5 % Zr sample at 30 min, as can be seen in Figure 5.3. These observations confirm that grain growth is responsible for the observed hardness decrease.

Increasing Zr content seems to promote grain growth, as can be observed from Figure 4.16 as well. In the 5 % Zr composition, the hardening at 400 °C and 30 min is similar to 350 °C. In the 10 % Zr composition, it is slightly lower, while it is significantly lower for the 25 % Zr sample. In addition, the magnitude of hardness decrease at 500 and 600 °C increases with increasing Zr content. This can be explained by the decreasing melting point, which can be seen in Figure 5.4. According to Gubicza, the onset temperature for grain growth is directly linked to the melting point [22], which explains the larger extent of grain growth in the 25 % Zr sample.

A third mechanism

Finally, there is one more mechanism occuring during annealing, which the author believes to be precipitation of e.g. the α and/or ω phase, though there is no direct evidence. Such phenomenon is needed to fully explain the annealing behaviour of some samples. For example, consider Figure 4.10. There, it can be seen that at 350 °C, the hardness almost continuously increases, after the steep initial increase caused by anneal hardening. Similarly, the $(1\ 1\ 0)_\beta$ FWHM increases after an initial decrease caused by anneal hardening, which is even more so the case at 400 °C. At 600 °C, as can be seen in Figure 4.12, the $(1\ 1\ 0)_\beta$ FWHM also increases, though it is generally lower, which is presumably caused by grain growth.

The same is true in the other two compositions, as can be seen in Figure 4.14. Most interesting to consider is the 25 % Zr 350 °C curve. There, the initial hardness increase is strong, but grain growth rapidly offsets its effect. After two and four hours, however, the hardness somewhat recovers, presumably through this mechanism.

However, these phases have not been directly observed in the X-ray diffractograms. This means that the volume fraction of the second phase is rather low, though several authors have noted that, due to a large number of overlapping peaks, phase identification by XRD in these alloy systems is not straightforward, and complementary techniques may be necessary.

Despite the absence of second-phase peaks in the related diffractograms, Pang et al. [52] observed isothermal precipitation of the ω-phase in Ti-24Nb-6Zr (at.%), which has a similar composition to the 5 % Zr sample of this work (Ti-28Nb-5Zr (at.%)). In their case, after annealing coarse-grained alloy (40-50 µm), at 300 °C for 100 h, XRD, TEM and atom probe tomography all confirmed the presence of ω-precipitates, with ellipsoidal shape. Their length ranged between 2 and 8 nm. These precipitates caused a significant increase in Vickers hardness: from 155 HV1 as-cast, to about 290 HV1 after the 100 h annealing treatment. Furthermore, an annealing treatment of 1 h at same temperature already caused a hardness increase, to about 180 HV1, meaning precipitates already form at relatively short time scales. Similarly, Voelker et al. observed α-precipitates, sized about 50 nm, through TEM upon annealing UFG Ti-45Nb at 300 °C for 10 h (wt.%).

Another phenomenon that could have occurred is grain boundary segregation. There, certain alloying elements preferentially segregate to, or away from the grain boundary, though its effect on hardness is remains unclear [58]. Grain boundary segregation has been observed in β-Ti alloys by Pithriv et al. [57]. They, however, believe that the segregated atoms may play a role in the subsequent nucleation of α-phase at the grain boundary, which is observed in many Ti alloys [36].

In conclusion, based on findings in literature and observed continuous hardness increase during annealing, at timescales larger than the observed anneal hardening relaxation time, precipitation likely occurred in certain samples. There, however was no observations by XRD supporting this theory.

Chapter 6

Conclusion

This thesis evaluated the hardening effects of annealing on three high-pressure torsion (HPT) processed Ti-Nb-Zr alloys. We found that both HPT and subsequent annealing significantly strengthened the material. Specifically, HPT increased hardness by about 35 % compared to the as-cast state. Subsequent annealing at temperatures up to 400 or 500 °C resulted in further hardness increase. The annealing time effect on hardness change varied with annealing temperature: at low temperature, increasing annealing time further increased hardness, while at high temperature, grain growth caused hardness to decrease. Depending on composition, an additional hardening of 25 to 30 % relative to as-HPT hardness was possible.

Below the temperature threshold for grain growth, we observed linear hardening kinetics, which corresponds well to observations in the literature. The hardening kinetics, specifically the linear hardening rate was analyzed using the Arrhenius equation for thermally activated processes. We found that the activation energy for anneal hardening was around 0.1 - 0.15 eV, which is low compared to other alloy systems. Hence, we could exclude both lattice and grain boundary diffusion as rate-limiting process for anneal hardening. However, triple-junction diffusion could not be evaluated as potential mechanism, due to the lack of diffusion data. Hence, the responsible mechanism remains unidentified.

To identify the mechanism for anneal hardening in this βTi-alloys, future research should focus on temperature ranges $\leq 300\,^{\circ}\mathrm{C}$, to avoid grain growth interference. Additionally, the hardening rate should be determined based on the slope of a hardness-time curve, rather than using the assumption of 30 min used in this work. Furthermore, exploring anneal hardening in different β-Ti alloy systems, like Ti-Mo, could help further identify what role alloying elements play in anneal hardening.

Bibliography

[1] M. Abdel-Hady, H. Fuwa, K. Hinoshita, H. Kimura, Y. Shinzato, and M. Morinaga. Phase stability change with zr content in beta-type ti–nb alloys. *Scripta Materialia*, 57(11):1000–1003, 2007. doi:10.1016/j.scriptamat.2007.08.003.

[2] Argonne National Laboratory. Index of x0h database: characteristic x-ray lines. URL: https://x-server.gmca.aps.anl.gov/cgi/www_dbli.exe?x0hdb=waves.

[3] M. A. Atwater, H. Bahmanpour, R. O. Scattergood, and C. C. Koch. The thermal stability of nanocrystalline cartridge brass and the effect of zirconium additions. *Journal of Materials Science*, 48(1):220–226, 2013. doi:10.1007/s10853-012-6731-5.

[4] K. Bartha. *Phase transformations in ultra-fine grained titanium alloys*. Doctoral thesis, Charles University, 2019.

[5] M. Bönisch, M. Calin, J. van Humbeeck, W. Skrotzki, and J. Eckert. Factors influencing the elastic moduli, reversible strains and hysteresis loops in martensitic ti-nb alloys. *Materials science & engineering. C, Materials for biological applications*, 48:511–520, 2015. doi:10.1016/j.msec.2014.12.048.

[6] M. Bönisch, M. Calin, T. Waitz, A. Panigrahi, M. Zehetbauer, A. Gebert, W. Skrotzki, and J. Eckert. Thermal stability and phase transformations of martensitic ti–nb alloys. *Science and Technology of Advanced Materials*, 14(5):055004, 2013. doi:10.1088/1468-6996/14/5/055004.

[7] M. Bönisch, A. Panigrahi, M. Stoica, M. Calin, E. Ahrens, M. Zehetbauer, W. Skrotzki, and J. Eckert. Giant thermal expansion and alpha-precipitation pathways in ti-alloys. *Nature Communications*, 8(1), 2017. doi:10.1038/s41467-017-01578-1.

[8] M. Bönisch, M. Stoica, and M. Calin. Routes to control diffusive pathways and thermal expansion in ti-alloys. *Scientific reports*, 10(1):3045, 2020. doi:10.1038/s41598-020-60038-x.

[9] R. R. Boyer and R. D. Briggs. The use of beta titanium alloys in the aerospace industry. *Journal of Materials Engineering and Performance*, 14(6):681–685, 2005. doi:10.1361/105994905X75448.

[10] Y. Cao, S. Ni, X. Liao, M. Song, and Y. Zhu. Structural evolutions of metallic materials processed by severe plastic deformation. *Materials Science and Engineering: R: Reports*, 133:1–59, 2018. doi:10.1016/j.mser.2018.06.001.

[11] H. Chr, P. T. Wilger T, F. Hisker, and S. Divinski. Titanium tracer diffusion in grain boundaries of a-ti, a2-ti3al, and y-tial and in a2/y interphase boundaries. *Intermetallics*, (9):431–442, 2001.

[12] H. Conrad and J. Narayan. On the grain size softening in nanocrystalline materials. *Scripta Materialia*, 42(11):1025–1030, 2000. doi:10.1016/S1359-6462(00)00320-1.

[13] J. D. Cotton, R. D. Briggs, R. R. Boyer, S. Tamirisakandala, P. Russo, N. Shchetnikov, and J. C. Fanning. State of the art in beta titanium alloys for airframe applications. *JOM*, 67(6):1281–1303, 2015. doi:10.1007/s11837-015-1442-4.

[14] K. Edalati and Z. Horita. A review on high-pressure torsion (hpt) from 1935 to 1988. *Materials Science and Engineering: A*, 652:325–352, 2016. doi:10.1016/j.msea.2015.11.074.

[15] D. Erb. pybaselines: A python library of algorithms for the baseline correction of experimental data. URL: https://github.com/derb12/pybaselines, doi:10.5281/zenodo.5608581.

[16] G. Faraji, H. S. Kim, and H. T. Kashi. Effective parameters for the success of severe plastic deformation methods. In *Severe Plastic Deformation*, pages 187–222. Elsevier, 2018. doi:10.1016/B978-0-12-813518-1.00006-0.

[17] G. Faraji, H. S. Kim, and H. T. Kashi. Introduction. In *Severe Plastic Deformation*, pages 1–17. Elsevier, 2018. doi:10.1016/B978-0-12-813518-1.00020-5.

[18] G. Faraji, H. S. Kim, and H. T. Kashi. Severe plastic deformation for industrial applications. In *Severe Plastic Deformation*, pages 165–186. Elsevier, 2018. doi:10.1016/B978-0-12-813518-1.00005-9.

[19] G. Faraji, H. S. Kim, and H. T. Kashi. Severe plastic deformation methods for bulk samples. In *Severe Plastic Deformation*, pages 37–112. Elsevier, 2018. doi:10.1016/B978-0-12-813518-1.00002-3.

[20] J. G. Ferrero. Candidate materials for high-strength fastener applications in both the aerospace and automotive industries. *Journal of Materials Engineering and Performance*, 14(6):691–696, 2005. doi:10.1361/105994905X75466.

[21] T. Fujioka and Z. Horita. Development of high-pressure sliding process for microstructural refinement of rectangular metallic sheets. *MATERIALS TRANSACTIONS*, 50(4):930–933, 2009. doi:10.2320/matertrans.MRP2008445.

[22] J. Gubicza. Annealing–induced hardening in ultrafine–grained and nanocrystalline materials. *Advanced Engineering Materials*, 22(1), 2020. doi:10.1002/adem.201900507.

[23] J. Gubicza, P. H. R. Pereira, G. Kapoor, Y. Huang, S. S. Vadlamani, and T. G. Langdon. Annealing–induced hardening in ultrafine–grained ni–mo alloys. *Advanced Engineering Materials*, 20(9), 2018. doi:10.1002/adem.201800184.

[24] E. O. Hall. The deformation and ageing of mild steel: Iii discussion of results. *Proceedings of the Physical Society. Section B*, 64(9):747–753, 1951. doi:10.1088/0370-1301/64/9/303.

[25] Y. Harai, Y. Ito, and Z. Horita. High-pressure torsion using ring specimens. *Scripta Materialia*, 58(6):469–472, 2008. doi:10.1016/j.scriptamat.2007.10.037.

[26] K. C. Hari Kumar, P. Wollants, and L. Delacy. Thermodynamic assessment of the ti-zr system and calculation of the nb-ti-zr phase diagram. *Journal of Alloys and Compounds*, 206(1):121–127, 1994. doi:10.1016/0925-8388(94)90019-1.

[27] C. R. Harris, K. J. Millman, S. J. van der Walt, R. Gommers, P. Virtanen, D. Cournapeau, E. Wieser, J. Taylor, S. Berg, N. J. Smith, R. Kern, M. Picus, S. Hoyer, M. H. van Kerkwijk, M. Brett, A. Haldane, J. Del Fernández Río, M. Wiebe, P. Peterson, P. Gérard-Marchant, K. Sheppard, T. Reddy, W. Weckesser, H. Abbasi, C. Gohlke, and T. E. Oliphant. Array programming with numpy. *Nature*, 585(7825):357–362, 2020. doi:10.1038/s41586-020-2649-2.

[28] D. W. Hoeppner and V. Chandrasekaran. Fretting in orthopaedic implants: A review. *Wear*, 173(1-2):189–197, 1994. doi:10.1016/0043-1648(94)90272-0.

[29] M. Hu, L. Wang, G. Li, Q. Huang, Y. Liu, J. He, H. Wu, and M. Song. Investigations on microstructure and properties of ti-nb-zr medium-entropy alloys for metallic biomaterials. *Intermetallics*, 145:107568, 2022. doi:10.1016/j.intermet.2022.107568.

[30] X. Huang, N. Hansen, and N. Tsuji. Hardening by annealing and softening by deformation in nanostructured metals. *Science (New York, N.Y.)*, 312(5771):249–251, 2006. doi:10.1126/science.1124268.

[31] J. D. Hunter. Matplotlib: A 2d graphics environment. *Computing in Science & Engineering*, 9(3):90–95, 2007. doi:10.1109/MCSE.2007.55.

[32] International Organization for Standardization. Metallic materials - vickers hardness test: Part 1: Test method, 2018.

[33] M. Janeček, J. Čížek, J. Stráský, K. Václavová, P. Hruška, V. Polyakova, S. Gatina, and I. Semenova. Microstructure evolution in solution treated ti15mo alloy processed by high pressure torsion. *Materials Characterization*, 98:233–240, 2014. doi:10.1016/j.matchar.2014.10.024.

[34] G. Ji, Z. Zhou, F. Meng, X. Yang, R. Sheng, J. Qiao, P. K. Liaw, M. Li, L. Jiang, S. Chen, and Y. Tong. Effect of zr addition on the local structure and mechanical properties of ti–ta–nb–zr refractory high-entropy alloys. *Journal of Materials Research and Technology*, 19:4428–4438, 2022. doi:10.1016/j.jmrt.2022.06.160.

[35] H. Y. Kim and S. Miyazaki. Martensitic transformation and superelastic properties of ti-nb base alloys. *MATERIALS TRANSACTIONS*, 56(5):625–634, 2015. doi:10.2320/matertrans.M2014454.

[36] R. Kolli and A. Devaraj. A review of metastable beta titanium alloys. *Metals*, 8(7):506, 2018. doi:10.3390/met8070506.

[37] S. V. Konushkin, M. I. Baskakova, A. V. Leonov, E. O. Nasakina, M. A. Sudarchikova, A. A. Kolmakova, A. Bespamiatnova, K. V. Sergiyenko, Y. O. Leonova, and M. A. Sevostyanov. The structure of the alloy ti - (20-30) nb - 5zr after smelting and homogenizing annealing. *IOP Conference Series: Materials Science and Engineering*, 525:012060, 2019. doi:10.1088/1757-899X/525/1/012060.

[38] P. Kovacs and J. A. Davidson. The electrochemical behavior of a new titanium alloy with superior biocompatibity. *Titanium'92 Science and Technology*, pages 2705–2712, 1993.

[39] T. A. Latynina, A. M. Mavlyutov, M. Y. Murashkin, R. Z. Valiev, and T. S. Orlova. The effect of hardening by annealing in ultrafine-grained al–0.4zr alloy: influence of zr microadditives. *Philosophical Magazine*, 99(19):2424–2443, 2019. doi:10.1080/14786435.2019.1631501.

[40] S.-W. Lee, S. M. Han, and W. D. Nix. Uniaxial compression of fcc au nanopillars on an mgo substrate: The effects of prestraining and annealing. *Acta Materialia*, 57(15):4404–4415, 2009. doi:10.1016/j.actamat.2009.06.002.

[41] H. Li, P. Wang, and C. Wen. Recent progress on nanocrystalline metallic materials for biomedical applications. *Nanomaterials (Basel, Switzerland)*, 12(12), 2022. doi:10.3390/nano12122111.

[42] X. Z. Liao, A. R. Kilmametov, R. Z. Valiev, H. Gao, X. Li, A. K. Mukherjee, J. F. Bingert, and Y. T. Zhu. High-pressure torsion-induced grain growth in electrodeposited nanocrystalline ni. *Applied Physics Letters*, 88(2), 2006. doi:10.1063/1.2159088.

[43] M. Long and H. J. Rack. Titanium alloys in total joint replacement–a materials science perspective. *Biomaterials*, 19(18):1621–1639, 1998. doi:10.1016/S0142-9612(97)00146-4.

[44] A. M. Mavlyutov, A. S. Bondarenko, M. Murashkin, E. V. Boltynjuk, R. Z. Valiev, and T. S. Orlova. Effect of annealing on microhardness and electrical

resistivity of nanostructured spd aluminium. *Journal of Alloys and Compounds*, 698:539–546, 2017. doi:10.1016/j.jallcom.2016.12.240.

[45] A. Mehjabeen, W. Xu, D. Qiu, and M. Qian. Redefining the beta-phase stability in ti-nb-zr alloys for alloy design and microstructural prediction. *JOM*, 70(10):2254–2259, 2018. doi:10.1007/s11837-018-3010-1.

[46] M. A. Meyers, A. Mishra, and D. J. Benson. Mechanical properties of nanocrystalline materials. *Progress in Materials Science*, 51(4):427–556, 2006. doi:10.1016/j.pmatsci.2005.08.003.

[47] D. L. Moffat. *Phase transformations in the titanium-niobium binary alloy system*. Doctoral thesis, University Of Wisconsin - Madison, 1985. URL: https://www.osti.gov/biblio/5429759,journal=.

[48] E. K. Molchanova. Phase diagrams of titanium alloys. *Israel Program for Scientific Translations*, pages 153–158, 1965.

[49] D. C. Montgomery, G. C. Runger, and N. F. Hubele. *Engineering statistics*. John Wiley, Hoboken NJ, 5th ed. edition, 2011.

[50] M. Newville, T. Stensitzki, D. B. Allen, and A. Ingargiola. Lmfit: Non-linear least-square minimization and curve-fitting for python, 2014. doi:10.5281/zenodo.11813.

[51] M. Niinomi and M. Nakai. Titanium-based biomaterials for preventing stress shielding between implant devices and bone. *International journal of biomaterials*, 2011:836587, 2011. doi:10.1155/2011/836587.

[52] E. L. Pang, E. J. Pickering, S. I. Baik, D. N. Seidman, and N. G. Jones. The effect of zirconium on the omega phase in ti-24nb-[0–8]zr (at.%) alloys. *Acta Materialia*, 153:62–70, 2018. doi:10.1016/j.actamat.2018.04.016.

[53] A. Panigrahi, M. Bönisch, T. Waitz, E. Schafler, M. Calin, J. Eckert, W. Skrotzki, and M. Zehetbauer. Phase transformations and mechanical properties of biocompatible ti–16.1nb processed by severe plastic deformation. *Journal of Alloys and Compounds*, 628:434–441, 2015. doi:10.1016/j.jallcom.2014.12.159.

[54] N. J. Petch. The cleavage strength of polycrystals. *Journal of the Iron and Steel Institute*, 174:25–28, 1953.

[55] R. Pippan, S. Scheriau, A. Hohenwarter, and M. Hafok. Advantages and limitations of hpt: A review. *Materials Science Forum*, 584-586:16–21, 2008. doi:10.4028/www.scientific.net/MSF.584-586.16.

[56] R. Pippan, S. Scheriau, A. Taylor, M. Hafok, A. Hohenwarter, and A. Bachmaier. Saturation of fragmentation during severe plastic deformation. *Annual Review of Materials Research*, 40(1):319–343, 2010. doi:10.1146/annurev-matsci-070909-104445.

[57] T. S. Prithiv, Z. Kloenne, D. Li, R. Shi, Y. Zheng, H. L. Fraser, B. Gault, and S. Antonov. Grain boundary segregation and its implications regarding the formation of the grain boundary alpha phase in the metastable beta-titanium ti–5al–5mo–5v–3cr alloy. *Scripta Materialia*, 207:114320, 2022. doi:10.1016/j.scriptamat.2021.114320.

[58] O. Renk, A. Hohenwarter, K. Eder, K. S. Kormout, J. M. Cairney, and R. Pippan. Increasing the strength of nanocrystalline steels by annealing: Is segregation necessary? *Scripta Materialia*, 95:27–30, 2015. doi:10.1016/j.scriptamat.2014.09.023.

[59] O. Renk and R. Pippan. Transition from thermally assisted to mechanically driven boundary migration and related apparent activation energies. *Scripta Materialia*, 154:212–215, 2018. doi:10.1016/j.scriptamat.2018.05.052.

[60] O. Renk and R. Pippan. Anneal hardening in single phase nanostructured metals. *MATERIALS TRANSACTIONS*, 64(7):1464–1473, 2023. doi:10.2320/matertrans.MT-MF2022029.

[61] T. J. Rupert, J. R. Trelewicz, and C. A. Schuh. Grain boundary relaxation strengthening of nanocrystalline ni–w alloys. *Journal of Materials Research*, 27(9):1285–1294, 2012. doi:10.1557/jmr.2012.55.

[62] R. Santhosh, M. Geetha, and M. Nageswara Rao. Recent developments in heat treatment of beta titanium alloys for aerospace applications. *Transactions of the Indian Institute of Metals*, 70(7):1681–1688, 2017. doi:10.1007/s12666-016-0985-6.

[63] P. M. Sargent and M. F. Ashby. Deformation maps for titanium and zirconium. *Scripta Metallurgica*, 16(12):1415–1422, 1982.

[64] A. Thoemmes, I. A. Bataev, D. V. Lazurenko, A. A. Ruktuev, I. V. Ivanov, C. Afonso, A. Stark, and A. M. Jorge Jr. Microstructure and lattice parameters of suction-cast ti–nb alloys in a wide range of nb concentrations. *Materials Science and Engineering: A*, 818:141378, 2021. doi:10.1016/j.msea.2021.141378.

[65] T. Ungár and G. Ribárik. Characterization of ufg materials by x-ray and neutron diffraction. *IOP Conference Series: Materials Science and Engineering*, 194:012003, 2017. doi:10.1088/1757-899X/194/1/012003.

[66] R. Valiev, R. Islamgaliev, and I. Alexandrov. Bulk nanostructured materials from severe plastic deformation. *Progress in Materials Science*, 45(2):103–189, 2000. doi:10.1016/S0079-6425(99)00007-9.

[67] R. Z. Valiev, Y. Ivanisenko, E. F. Rauch, and B. Baudelet. Structure and deformaton behaviour of armco iron subjected to severe plastic deformation. *Acta Materialia*, 44(12):4705–4712, 1996. doi:10.1016/S1359-6454(96)00156-5.

[68] H. van Swygenhoven, P. M. Derlet, and A. G. Frøseth. Nucleation and propagation of dislocations in nanocrystalline fcc metals. *Acta Materialia*, 54(7):1975–1983, 2006. doi:10.1016/j.actamat.2005.12.026.

[69] B. Völker, N. Jäger, M. Calin, M. Zehetbauer, J. Eckert, and A. Hohenwarter. Influence of testing orientation on mechanical properties of ti45nb deformed by high pressure torsion. *Materials & Design*, 114:40–46, 2017. doi:10.1016/j.matdes.2016.10.035.

[70] A. Vorhauer and R. Pippan. On the homogeneity of deformation by high pressure torsion. *Scripta Materialia*, 51(9):921–925, 2004. doi:10.1016/j.scriptamat.2004.04.025.

[71] B. Yang, H. Vehoff, A. Hohenwarter, M. Hafok, and R. Pippan. Strain effects on the coarsening and softening of electrodeposited nanocrystalline ni subjected to high pressure torsion. *Scripta Materialia*, 58(9):790–793, 2008. doi:10.1016/j.scriptamat.2007.12.039.

[72] H. Yilmazer, M. Niinomi, M. Nakai, K. Cho, J. Hieda, Y. Todaka, and T. Miyazaki. Mechanical properties of a medical beta-type titanium alloy with specific microstructural evolution through high-pressure torsion. *Materials science & engineering. C, Materials for biological applications*, 33(5):2499–2507, 2013. doi:10.1016/j.msec.2013.01.056.

[73] H. Yilmazer, M. Niinomi, M. Nakai, J. Hieda, Y. Todaka, T. Akahori, and T. Miyazaki. Heterogeneous structure and mechanical hardness of biomedical beta-type ti-29nb-13ta-4.6zr subjected to high-pressure torsion. *Journal of the mechanical behavior of biomedical materials*, 10:235–245, 2012. doi:10.1016/j.jmbbm.2012.02.022.

[74] T. Yu, N. Hansen, X. Huang, and A. Godfrey. Observation of a new mechanism balancing hardening and softening in metals. *Materials Research Letters*, 2(3):160–165, 2014. doi:10.1080/21663831.2014.886308.

[75] J. Zhang, R. Rynko, J. Frenzel, C. Somsen, and G. Eggeler. Ingot metallurgy and microstructural characterization of ti–ta alloys. *International Journal of Materials Research*, 105(2):156–167, 2014. doi:10.3139/146.111010.

[76] J. Zhang, F. Sun, Y. Hao, N. Gozdecki, E. Lebrun, P. Vermaut, R. Portier, T. Gloriant, P. Laheurte, and F. Prima. Influence of equiatomic zr/nb substitution on superelastic behavior of ti–nb–zr alloy. *Materials Science and Engineering: A*, 563:78–85, 2013. doi:10.1016/j.msea.2012.11.045.

[77] X. Zhang, Y. Chen, and J. Hu. Recent advances in the development of aerospace materials. *Progress in Aerospace Sciences*, 97:22–34, 2018. doi:10.1016/j.paerosci.2018.01.001.

[78] Y. Zhang, H. Liu, and Z. Jin. Thermodynamic assessment of the nb-ti system. *Calphad*, 25(2):305–317, 2001. doi:10.1016/S0364-5916(01)00051-7.